microRNA-138 controls hippocampal interneuron function and short-term memory

Daswani, R.[1], Gilardi, C.[1], Soutschek, M.[1], Nanda, P.[1], Weiss, K.[2], Bicker, S.[1], Fiore, R.[1], Dieterich, C.[3], Germain, P.L.[1], Winterer, J*[1], Schratt, G*[1].

[1]Lab of Systems Neuroscience, Institute for Neuroscience, Department of Health Science and Technology, Swiss Federal Institute of Technology ETH, 8057 Zurich, Switzerland

[2]Institute for Physiological Chemistry, Biochemical-Pharmacological Center Marburg, Philipps-University of Marburg, 35032 Marburg, Germany

[3]Section of Bioinformatics and Systems Cardiology, Department of Internal Medicine III and Klaus Tschira Institute for Integrative Computational Cardiology, University of Heidelberg, Germany

*co-corresponding authors: jochen.winterer@hest.ethz.ch; gerhard.schratt@hest.ethz.ch

Keywords: microRNA, interneuron, inhibitory synapse, working memory, schizophrenia

Abstract

The proper development and function of neuronal circuits relies on a tightly regulated balance between excitatory and inhibitory (E/I) synaptic transmission, and disrupting this balance can cause neurodevelopmental disorders, e.g. schizophrenia. microRNA-dependent gene regulation in pyramidal neurons is important for excitatory synaptic function and cognition, but its role in inhibitory interneurons is poorly understood. Here, we identify miR-138-5p as a regulator of short-term memory and inhibitory synaptic transmission in the hippocampus. Sponge-mediated miR-138-5p inactivation specifically in parvalbumin (PV)-expressing interneurons impairs spatial recognition memory and enhances GABAergic synaptic input onto pyramidal neurons. Cellular and behavioural phenotypes associated with miR-138-5p inactivation are paralleled by an upregulation of the schizophrenia-associated *Erbb4*, which we validated as a direct miR-138-5p target gene. Our findings suggest that miR-138-5p is a critical regulator of PV interneuron function, with implications for cognition and schizophrenia. More generally, they provide evidence that microRNAs orchestrate neural circuit development by fine-tuning both excitatory and inhibitory synaptic transmission.

Introduction

microRNAs (miRNAs) are short non-coding RNAs which act as negative regulators of mRNA translation and stability (Bartel, 2018). Over the last decade, a large body of evidence shows that miRNAs control excitatory neuron development, function and plasticity (McNeill and Van Vactor, 2012; Schratt, 2009). Specific miRNAs, e.g. miR-132, -134 and -138, have been identified which control dendritic spines, the major sites of excitatory synaptic contact (Schratt et al., 2006; Siegel et al., 2009). Complete lack of miRNAs from excitatory forebrain neurons in Dicer-deficient mice enhances learning and memory (Konopka et al., 2010), and specific miRNAs have been linked to both short-term and long-term memory regulation (Cheng et al., 2018; Gao et al., 2010; Walgrave et al., 2021). Although miRNAs are likewise substantially expressed in inhibitory γ-aminobutyric acid (GABA)ergic interneurons (He et al., 2012), relatively little is known about miRNA function in this cell-type. The complete lack of miRNAs reduces the number of cortical interneurons (Tuncdemir et al., 2015) while the absence of miRNAs in interneurons expressing vasoactive intestinal peptide (VIP) leads to cortical circuit dysfunction (Qiu et al., 2020). miR-128 knockout in Drd1a-positive GABAergic medium spiny neurons of the striatum results in increased motor activity and fatal epilepsy (Tan et al., 2013).

In the rodent hippocampus, microcircuits of excitatory pyramidal neurons and local inhibitory interneurons provide an extensively studied model in the context of information processing, with specific implications for the control of spatial short-term and long-term memory (Booker and Vida, 2018; Markram et al., 2004; Pelkey et al., 2017). Among the different interneuron classes, fast-spiking parvalbumin (PV) expressing interneurons play a particularly prominent role in controlling pyramidal neuron output to drive appropriate behavioral responses (Murray et al., 2011; Rico and Marin, 2011). For example, CA1 PV interneurons are required for spatial working memory, but neither for reference memory nor for memory acquisition in contextual fear conditioning (CFC) (Fuchs et al., 2007; Lovett-Barron et al., 2014; Murray et al., 2011). PV interneuron dysfunction has been implicated in neuropsychiatric disorders, most notably schizophrenia, but also epilepsy and autism-spectrum disorders (ASD) (Del Pino et al., 2018; Sohal and Rubenstein, 2019). However, the role of specific miRNAs in PV interneurons in the context of higher cognitive function is completely elusive.

77

Results

We previously identified the brain-enriched miR-138-5p as an important regulator of excitatory synapse function in hippocampal pyramidal neurons (Siegel et al., 2009). To study the role of miR-138-5p on a behavioral level, we generated mice with a conditional ROSA26 transgene (138-floxed) which allows expression of a miR-138-5p inactivating sponge transcript harboring a lacZ coding sequence and 6 imperfect miR-138-5p binding sites (6x-miR-138sponge) upon Cre-recombinase expression. Sponge transcripts sequester endogenous miRNA, thereby leading to miRNA inactivation and the de-repression of cognate target genes (Ebert and Sharp, 2010). 138-floxed mice without Cre transgene served as a control throughout the experiments. Since these control mice completely lack expression of any sponge-related transcript *in vivo*, we first carefully validated specificity and efficiency of the 138-sponge transcript in primary rat hippocampal neurons. Therefore, we compared the 138-sponge transcript to an identical control sponge, except that the 6 imperfect miR-138 binding sites were replaced with a shuffled sequence not supposed to sequester any miRNA expressed in neurons (cf. Methods). This analysis revealed a robust and specific inactivation of miR-138-5p by 138-sponge *in vitro* (**suppl. Fig. 1a, b, c**).

We then activated 138-sponge expression at embryonic stage *in vivo* by crossing 138-floxed mice to the ubiquitous Cre-driver line CMV-Cre (138-sponge^{ub}, **Fig. 1a**). lacZ staining revealed highly penetrant expression of 6x-miR-138 sponge in the hippocampus of 138-floxed mice upon CMV-Cre expression (**suppl. Fig. 1d**). To test for the degree of miR-138-5p inhibition *in vivo* we made use of a dual fluorescence miR-138 sensor virus which we injected into the hippocampus of 138-sponge^{ub} mice. Briefly, the sensor consists of a GFP coding sequence (cds) followed by two perfect miR-138 binding sites and a mCherry cds (suppl. Fig. 1e). Thus, the lower the ratio of GFP/mCherry, the higher the cellular miR-138 activity. Quantifying GFP/mCherry ratios over many infected neurons revealed that in neurons with 6x-miR-138-sponge expression, GFP/mCherry ratios were significantly higher compared to controls, indicative of an efficient sequestering of endogenous miR-138-5p by our sponge construct (**Fig. 1b**).

We next assessed cognitive abilities of 138-sponge^{ub} mice using behavioral testing. Locomotion in the home cage was similar between 138-sponge^{ub} and control mice,

112 ruling out severe developmental motor impairments as a potential confound (**suppl.**
113 **Fig.1f**). In the Y-maze test, no genotype-dependent differences in spontaneous
114 alternations were observed, suggesting that exploratory behavior was not affected by
115 miR138-5p inactivation (**suppl. Fig. 1g**). In contrast, 138-sponge^{ub} mice displayed a
116 significant impairment in novelty preference (**Fig. 1c**), indicating a loss of spatial
117 short-term memory. In the novel object recognition (NOR) task, 138-sponge^{ub} mice
118 were unable to discriminate the novel from the familiar object (**Fig. 1d**), thereby
119 corroborating the observed short-term memory deficit. In contrast, associative long-
120 term memory, as assessed by classical fear conditioning (**Fig. 1e**), as well as
121 anxiety-related behavior (open field, EPM), was not affected by miR-138-5p inhibition
122 (**suppl. Fig. 1h, I, j**). Thus, ubiquitous miR-138-5p inhibition leads to a short-term
123 memory deficit.
124 We went on to test whether short-term memory impairments in 138-sponge^{ub} mice
125 were associated with alterations in synaptic transmission in hippocampal area CA1
126 and recorded miniature excitatory postsynaptic currents (mEPSCs) in CA1 pyramidal
127 neurons. Amplitude and frequency of mEPSCs were indistinguishable between 138-
128 sponge^{ub} and control slices (**Fig. 1f**, **suppl. Fig. 1k, 1l**). Likewise, we did not detect
129 any significant alterations in dendritic spine morphology in these neurons using Golgi
130 staining (**Fig. 1g**). Finally, we did not observe differences in paired-pulse ratio (PPR),
131 which negatively correlates with presynaptic release probability (**suppl. Fig. 1m**),
132 suggesting that excitatory synaptic transmission at the Schaffer collateral CA1
133 pyramidal cell synapse was not affected by miR-138-5p inhibition.
134 To identify miR-138-5p target mRNAs and to obtain further insight into the biological
135 function of miR-138-5p regulated genes, we performed polyA-RNA sequencing with
136 total RNA isolated from hippocampal tissue. Differential gene expression analysis
137 recovered a total of 338 differentially expressed genes (DEG; 265 upregulated, 73
138 downregulated) (FDR<0.05; **Fig. 2a**). The presence of miR-138-5p binding sites
139 correlated with increased transcript levels compared with 138-floxed mice (**Fig. 2b**).
140 miR-138-5p 7-mer 1a, and to a lesser extent 7mer-m8 and 8mer sites, predicted
141 significant de-repression (**suppl. Fig. 2a**). In total, 56 (21%) of the upregulated, but
142 only 6 (8%) of the downregulated genes harbor miR-138-5p binding sites within their
143 3'UTR. Together, this data demonstrates that many of the observed upregulated
144 genes are a direct consequence of miR-138-5p inhibition and further confirms the
145 specificity of the miR-138-5p sponge transgene.

146 Gene ontology (GO) term analysis on DEGs from the RNA-seq analysis (**Fig. 2c**;
147 **suppl. Fig. 2b**) revealed that many GO terms associated with synaptic function are
148 strongly over-represented in genes upregulated in the hippocampus of 138-sponge^{ub}
149 mice. In order to specify the origin for the observed gene expression changes, we
150 compared DEGs to single cell RNA-seq data from different cell types present in the
151 hippocampus (Zeisel et al., 2018) (**Fig. 2d, suppl. Fig. 2c**). Surprisingly, we found
152 that those genes which were significantly upregulated in 138-sponge^{ub} mice are
153 strongly enriched in inhibitory GABAergic interneurons. This finding is in line with the
154 observation that excitatory synaptic transmission in hippocampal CA1 was not
155 affected by miR-138-5p inactivation (**Fig. 1f, g**, **suppl. Fig. 1 j-l**). Accordingly, many
156 of the upregulated miR-138-5p targets showed a strong expression signal in different
157 classes of inhibitory interneurons (**suppl. Fig. 2d**). In contrast, known validated
158 targets of miR-138-5p which are not enriched in inhibitory interneurons (e.g., Lypla1,
159 Sirt1, Fmr1) were not differentially expressed between 138-sponge^{ub} and control
160 mice (**suppl. Fig. 2e**).
161 Next, we performed single-molecule miRNA FISH in cultured rat hippocampal
162 neurons to visualize miR-138-5p expression at subcellular resolution. This analysis
163 revealed strong expression of miR-138-5p in both Camk2a-positive excitatory and
164 Erbb4-positive inhibitory hippocampal neurons (**Fig. 3a**). Erbb4-positive cells
165 express Gad65, but not Camk2a, confirming their GABAergic phenotype (**Fig. 3a**).
166 Quantification of the FISH signal didn't reveal any significant differences in the
167 average cellular miR-138-5p expression between excitatory and inhibitory neurons
168 (**suppl. Fig. 3a**), in agreement with an analysis of published miRNA-seq data from
169 the mouse cortex (**suppl. Fig. 3b**) (He et al., 2012). In contrast, miR-138-5p
170 expression was undetectable in GFAP-positive glial cells (**suppl. Fig. 3c**). Thus,
171 miR-138-5p is robustly expressed in inhibitory interneurons, consistent with a
172 previously unrecognized function in these cells.
173 We went on to validate miR-138-5p dependent regulation of predicted interneuron-
174 enriched target genes, focusing on Erbb4 (Erb-B2 receptor tyrosine kinase 4). Erbb4
175 is a SCZ risk gene which has been linked to the regulation of GABAergic synaptic
176 transmission and short-term memory (Fazzari et al., 2010; Wang et al., 2018). Using
177 qPCR and Western blot, we observed a significant upregulation of both Erbb4 mRNA
178 **(Fig. 3b)** and protein **(Fig. 3c)** levels in the hippocampus of 138-sponge^{ub} compared
179 to 138-floxed mice, thereby validating our results from RNA-seq. On the other hand,

180 transfection of primary rat hippocampal neurons with a synthetic miR-138-5p mimic
181 reduced Erbb4 protein levels **(Fig. 3d)**, demonstrating that miR-138-5p is necessary
182 and sufficient for the inhibition of Erbb4 expression. In luciferase reporter gene
183 assays, transfection of miR-138-5p significantly reduced the expression of an Erbb4
184 3'UTR construct containing a wild-type, but not mutant miR-138-5p binding site (**Fig.**
185 **3e**), rendering Erbb4 as direct miR-138-5p target. Furthermore, we were able to
186 validate the presynaptic vesicle associated Rims3 as an interneuron-enriched miR-
187 138-5p target **(suppl. Fig. 3d-f)**.
188 To study the regulation of Erbb4 by miR-138-5p specifically in interneurons, we
189 designed a viral construct in which expression of an inhibitory miR-138 sponge or a
190 respective control sponge is under the control of the interneuron-specific Dlx5/6
191 promoter (Dlx-138-sponge, Dlx-control sponge). rAAV expressing Dlx-138- or control
192 sponge co-localizes with Gad65/67 in primary rat hippocampal neurons, confirming
193 interneuron-specific expression **(suppl. Fig. 3g)**. Erbb4 RNA based on smFISH was
194 significantly elevated in Dlx-138-sponge compared to Dlx-control sponge infected
195 interneurons **(Fig. 3f)**, demonstrating that miR-138-5p cell-autonomously inhibits
196 Erbb4 expression in hippocampal interneurons.
197 Our experiments so far suggest that impairments in interneurons are causally
198 involved in short-term memory deficits upon miR-138 inhibition. To address the
199 hypothesis that the observed short-term deficits are hippocampus-dependent, we
200 stereotactically injected Dlx-138-sponge or Dlx control sponge into the dorsal
201 hippocampus of young adult mice and assessed short-term memory 4 weeks later,
202 as described. Specific expression of 138- and control-sponge in hippocampal
203 interneurons was confirmed by immunostaining **(Fig. 4a)**. The previously observed
204 138-sponge mediated impairments in Y-maze novel preference and NOR were fully
205 recapitulated by this approach **(Fig. 4b, 4c)**, strongly suggesting that miR-138-5p
206 function in hippocampal interneurons is required for intact short-term memory.
207 Importantly, short-term memory was fully preserved upon hippocampal interneuron-
208 specific expression of the control sponge **(Fig. 4b, 4c)**, providing an independent
209 confirmation of the specificity of our approach for miR-138-5p inactivation.
210 Next, we investigated electrophysiological alterations that might underlie the
211 observed short-term memory deficits. In hippocampal CA1 pyramidal neurons, which
212 are the main targets of PV-positive (PV+) interneurons in the hippocampal circuit,
213 frequency of miniature inhibitory postsynaptic current (mIPSC) was significantly

214 increased in mice injected with the Dlx-138-sponge as compared to control sponge
215 injected mice **(Fig. 4d)**. In contrast, amplitude **(Fig. 4e, suppl. Fig. 4a)** as well as
216 rise- and decay time **(suppl. Fig. 4b)** of mIPSCs was unaltered.
217 Based on this observation, we speculated that miR-138-5p inactivation might be
218 more robust in PV+ interneurons compared to other cell types. Thus, we again
219 injected a miR-138 pbds sensor construct into the hippocampus of control or miR-
220 138 sponge^{Ub} mice (cf. Fig. 1b), but now counterstained for parvalbumin (PV) to
221 quantify miR-138 activity in PV+ and PV- cells **(suppl. Fig. 4c)**. Analysis of
222 GFP/mCherry ratios revealed that expression of a miR-138 sponge significantly
223 inactivated miR-138-5p in PV+ neurons but had only a marginal effect in PV- cells
224 (which predominantly consist of excitatory pyramidal neurons). Thus, the observed
225 lack of regulation of miR-138-5p targets in excitatory pyramidal neurons of 138-
226 sponge^{Ub} mice is likely a result of inefficient sponge-mediated miR-138-5p inhibition
227 in this cell type. Since miR-138-5p and alterations in PV+ interneuron function had
228 recently been linked to schizophrenia (SCZ) (Pelkey et al., 2017; Watanabe et al.,
229 2014), we performed a comparison between DEGs from 138-sponge^{ub} mouse
230 hippocampus and cortical tissue of SCZ patients (Gandal et al., 2018). We found a
231 significant overlap between genes upregulated in the 138-sponge^{ub} hippocampus
232 and SCZ patients (p=0.00884; **suppl. Fig. 4d**). Taken together, our results suggest
233 that miR-138-5p inactivation due to expression of a miR-138 sponge predominantly
234 affects PV+ interneurons leading to an upregulation of synaptic genes which are
235 deregulated in SCZ.
236 To elaborate on the functional role of miR-138-5p in PV+ interneurons, we generated
237 138-sponge^{PV} mice by crossing 138-floxed mice to PV-Cre mice (**Fig. 5a**). In 138-
238 sponge^{PV} mice, the 6x-miR-138-sponge transcript is selectively expressed in the
239 majority (about 90%) of PV-expressing inhibitory interneurons (PV-positive cells)
240 (**Fig. 5b**). On a behavioral level, we found that locomotion and anxiety-related
241 behavior, as measured in the open field and EPM tests, was unaltered in 138-
242 sponge^{PV} mice compared to their littermate controls (**suppl. Fig. 5a-c**). However,
243 similar as 138-sponge^{ub} mice (**Fig. 1c, d**) and mice injected with rAAV-Dlx5/6-138-
244 sponge into the hippocampus **(Fig. 4b, c)**, 138-sponge^{PV} mice showed impairments
245 in behavioral tasks addressing short-term memory, such as the Y-maze novelty
246 preference (**Fig. 5c**) and NOR (**Fig. 5d**) tests. No genotype-dependent differences in
247 spontaneous alternations in the Y-maze were observed (**Fig 5e**). Similar to 138-

248 sponge^{ub} mice, associative long-term memory as assessed by conditional fear
249 conditioning was not affected in 138-sponge^{PV} mice **(suppl. Fig. 5d)**. These results
250 demonstrate that miR-138-5p activity in PV-positive interneurons is required to
251 sustain proper short-term memory. Next, we investigated electrophysiological
252 alterations that might underlie the observed short-term memory deficits. In
253 hippocampal CA1 pyramidal neurons of 138-sponge^{PV} mice, similar to rAAV-Dlx5/6-
254 138-sponge injected mice, frequency of miniature inhibitory postsynaptic current
255 (mIPSC) was significantly increased in 138-sponge^{PV} as compared to control slices
256 (**Fig. 6a**, **suppl. Fig. 6**), while neither amplitude, nor rise or decay time were
257 changed (**suppl. Fig. 6b-d**). The total number of PV-positive interneurons in the
258 hippocampus was similar between 138-sponge^{PV} and 138-floxed mice (**suppl. Fig.
259 6e**), suggesting that mIPSC frequency changes either result from an increased
260 number of inhibitory presynaptic boutons synapsing onto pyramidal cells or an
261 enhanced neurotransmitter release. To distinguish between these possibilities, we
262 first analyzed presynaptic boutons contacting CA1 pyramidal cells by staining slices
263 obtained from 138-floxed and 138-sponge^{PV} mice with antibodies against PV and the
264 vesicular GABA transporter (VGAT). Our analysis revealed no significant difference
265 in the number and intensity of PV-positive presynaptic boutons impinging onto the
266 somata of CA1 pyramidal cells between 138-sponge^{PV} mice and their littermate
267 controls (**Fig.6b**). To probe for changes in presynaptic release probability, we first
268 recorded extracellularly stimulated inhibitory paired-pulse ratios (iPPRs) in CA1
269 pyramidal cells but did not observe differences between the two groups (**Fig. 6c**).
270 Finally, we performed paired whole-cell recordings between presynaptic putative
271 fast-spiking PV-positive interneurons in stratum pyramidale and postsynaptic CA1
272 pyramidal cells **(Fig. 6d-f; suppl. Fig. 6f)**. The analysis of unitary connections
273 revealed increased, albeit not significant, uIPSC amplitudes (including failures of
274 transmission) and success rates (i.e., an action potential elicits an IPSC) in 138-
275 sponge^{PV} mice as compared to their control littermates (**Fig. 6d**). However, we did
276 not observe significant changes in paired-pulse ratio (**Fig. 6e**). Our further analysis
277 though revealed a significant decrease of the coefficient of variation (CV), indicative
278 of more reliable unitary synaptic connections between PV-positive interneurons and
279 CA1 pyramidal neurons in 138-sponge^{PV} mice (**Fig. 6f**). These findings may also
280 explain why mIPSC frequency was found to be altered as these inhibitory currents
281 reflect inputs of many GABAergic neurons onto a single excitatory pyramidal neuron.

282 In conclusion, CA1 pyramidal neurons in 138-sponge^{PV} mice receive increased
283 inhibitory GABAergic synaptic input from putative fast-spiking PV-positive
284 interneurons without detectable changes in perisomatic inhibitory bouton density or
285 size.
286
287 **Discussion**
288
289 Here, we describe a central role for the brain-enriched miRNA miR-138-5p in the
290 regulation of inhibitory GABAergic transmission in the hippocampus. Particularly, we
291 find that cell type-specific inhibition of miR-138-5p in PV-positive interneurons
292 enhances the reliability of unitary synaptic connections from putative fast-spiking PV-
293 positive interneurons onto CA1 pyramidal neurons. The resulting increase in
294 neurotransmitter release at this synapse is possibly due to an increase in the number
295 of presynaptic release sites within individual boutons (Sakamoto et al., 2018), as we
296 observed a decrease in CV, but did not detect significant changes in release
297 probability. PV-positive interneurons are the main source of feedforward inhibition
298 onto pyramidal neurons (Pouille and Scanziani, 2001) and have been functionally
299 linked to working memory (Murray et al., 2011), possibly via controlling gamma
300 oscillations (Hajos et al., 2004). We therefore propose a model whereby miR-138-5p
301 activity in PV+ interneurons is regulating neurotransmitter release, thereby keeping
302 pyramidal cell output in a range required for proper information processing. Since
303 miR-138-5p controls dendritic spine morphogenesis in cultured hippocampal
304 pyramidal neurons (Siegel et al., 2009), it might further regulate E-I balance in the
305 hippocampal circuitry by controlling pyramidal neuron excitatory input. The absence
306 of changes in excitatory synaptic transmission in the hippocampus of 138-sponge^{ub}
307 mice might be due to ineffective silencing of the highly abundant miR-138-5p in
308 pyramidal neurons via our approach. This view is supported by our observation that
309 a miR-138-5p sensor plasmid is effectively unsilenced in PV+, but not PV-
310 hippocampal neurons of 138-sponge^{ub} mice (suppl. Fig. 4d) and by the lack of
311 upregulation of miR-138-5p targets preferentially expressed in pyramidal neurons
312 (suppl. Fig. 2c). The molecular explanation for this PV-specific miR-138-5p
313 inactivation is currently unknown.
314 Sponge-mediated inactivation of miRNAs is routinely used in cell culture, but studies
315 employing this approach in transgenic mice are still scarce (Giusti et al., 2014),

316 possibly in part because a stringent control would require the generation of an
317 independent transgenic line. Here we addressed this issue by comparing the effects
318 of miR-138-sponge to a highly similar, but ineffective control sponge, in primary
319 neurons *in vitro* and in the hippocampus *in vivo* using multiple assays. Thereby, we
320 reproducibly observed 138-sponge specific effects on reporter gene expression
321 (suppl. Fig. 1b), dendritic spine size (suppl. Fig. 1c), miniature inhibitory postsynaptic
322 currents (Fig. 4d, e) and short-term memory (Fig. 4b, c), strongly arguing that the
323 effects seen in miR-138-sponge mice are due to miR-138-5p inactivation.
324 The molecular mechanisms downstream of miR-138-5p inactivation leading to
325 enhanced inhibition remain to be elucidated, but likely involve upregulation of
326 proteins organizing inhibitory synapse function. An interesting candidate in this
327 regard represents Erbb4, which has been shown to control GABAergic transmission
328 (Fazzari et al., 2010; Wang et al., 2018) and working memory (Tian et al., 2017; Wen
329 et al., 2010). In particular, release probability of GABAergic synapses onto pyramidal
330 neurons was diminished in Erbb4 KO mice (Wang et al., 2018), which is in
331 agreement with our finding that elevated Erbb4 levels in miR-138 sponge mice are
332 paralleled by higher mIPSC frequencies. However, additional presynaptic genes
333 might function downstream of miR-138-5p, e.g. Rims3, which physically and
334 functionally interacts with presynaptic voltage-dependent Ca^{2+} channels (VDCCs)
335 and increases neurotransmitter release (Takada et al., 2015). In the future, restoring
336 the expression of specific inhibitory presynaptic genes in miR-138 sponge mice will
337 be needed to assess their contribution to cellular and behavioural phenotypes
338 caused by miR-138 inhibition.
339 Intriguingly, interfering with miR-138-5p in inhibitory neurons of the adult
340 hippocampus fully recapitulates deficits in inhibitory synaptic transmission and short-
341 term memory observed in 138-sponge^{Ub} and 138-sponge^{PV} mice (Fig. 4). Although
342 this finding does not rule out a role for miR-138-5p at early stages of development, it
343 stresses the importance of miR-138-5p for the homeostasis of the fully developed
344 circuitry. A similar critical role at adulthood in the regulation of GABAergic
345 transmission and behavior was recently shown for the miR-138-5p target Erbb4
346 (Wang et al., 2018).
347 Our model of miR-138-5p being a positive regulator of memory is consistent with
348 results obtained from previous studies performed in mice (Boscher et al., 2020; Tatro
349 et al., 2013; Tian et al., 2018). Moreover, GWAS analysis identified miR-138-5p as a

350 putative regulator of human memory performance (Schroder et al., 2014). A rare
351 miR-138-2 gene variation is furthermore associated with SCZ in a Japanese
352 population (Watanabe et al., 2014), and miR-138-5p levels are altered in the superior
353 temporal gyrus and dorsolateral prefrontal cortex of SCZ patients (Beveridge et al.,
354 2010) (Moreau et al., 2011). Finally, several miR-138-5p targets have been
355 genetically linked to SCZ (e.g. *Erbb4, Drd2, Igsf9b*) (Kumar et al., 2010; Nicodemus
356 et al., 2006) or are deregulated in the cortex of SCZ patients (e.g. *Gabra3, Fxyd6,*
357 *Tmem132c*, *Baiap3*, suppl. Fig. 4d*)*. Thus, miR-138-5p might be involved in the
358 control of cognitive function in humans and represent a promising target for the
359 treatment of cognitive deficits associated with schizophrenia and other
360 neurodevelopmental disorders.
361

362 **Materials and methods**

Key Resources Table				
Reagent type (species) or resource	**Designation**	**Source or reference**	**Identifiers**	**Additional information**
Knock-in mouse line (mus musculus)	miR-138-flox	TaconicArtemis GmbH (Cologne, Germany)	C57BL/6NTac-*Gt(ROSA)26So* *tm2459(LacZ, antimir_138) Arte*	
Transgenic mouse line (mus musculus)	CMV-Cre	Jackson Laboratories	B6.C-Tg(CMV-Cre)1Cgn (CMV-CRE)	
Transgenic mouse line (mus musculus)	PV-Cre	Jackson Laboratories	B6;129P2-*Pvalb*$^{tm1(cre)Arbr}$/J (PV-CRE)	
DNA recombinant construct	Mir-138 sponge	MiR-138 sponge (modified pAAV-6P-SEWB backbone)		*MiR-138 sponge imperfect binding site*: 5' CGGCCTGATTCGTTCACCAGT 3'; spacer sequence: 5' TTTTT 3'; *Control sponge sequence*: 5' TGTGACTGGGGGCCAGAGG 3'; spacer sequence: 5' CAGTG 3'
DNA recombinant construct	AAV-Dlx5/6-miR-138 sponge	P199 from VVF and Addgene 83900)		
DNA recombinant construct	pGL3-138 perfect binding site (pbds) vector	pGL3 promotor vector (Promega, Mannheim)		*138 pbds reporter FW:* 5'CTAGACGGCCTGATTCACAACACCAGCTACCGGCCTGATTCACAACACCAGCTGGATCC 3' *138 pbds reporter REV:* 5'CTAGCGGATCCAGCTGGTGTTGTGAATCAGGCCGGTAGCTGGTGTTGTGAATCAGGCCGT 3'

DNA recombinant construct	AAV-miR-138 dual sensor construct	Addgene, 632524 Addgene, 114213		*138 perfect binding sites FW:* 5'CTAGACGGCCTGATTCACAACACCAGCTACCGGCCTGATTCACAACACCAGCTGGATCC 3' *138 perfect binding site REV:* 5'CTAGCGGATCCAGCTGGTGTTGTGAATCAGGCCGGTAGCTGGTGTTGTGAATCAGGCCGT 3'
Luciferase construct	PmirGlo Rims3 wt	pmirGLO dual-luciferase expression vector reporter (Promega, Madison, WI, USA)		5'GCCTCAGTCACCAGCTCTGTACCAGCAATACTCACCCCTCCACCTCCCTGACTT 3';
Luciferase construct	PmirGlo Rims3 138-mut	pmirGLO dual-luciferase expression vector reporter (Promega, Madison, WI, USA)		5'GCCTCAGTgAtatcCTCTGTACCAGCAATACTCACCCCTCCACCTCCCTGACTT 3';
Luciferase construct	PmirGlo ErbB4 wt	pmirGLO dual-luciferase expression vector reporter (Promega, Madison, WI, USA)		5'TTGAATGAAGCAATATGGAAGCAACCAGCAGATTAACTAATTTAAATACTTC 3';
Luciferase construct	PmirGlo ErbB4 138-mut	pmirGLO dual-luciferase expression vector reporter (Promega, Madison, WI, USA)		5'TTGAATGAAGCAATATGGAAGCAgCatGaAGATTAACTAATTTAAATACTTC 3';

Sequence based reagent	ErbB4 PCR primers (mmu)		PCR primers	FW 5'GACTCCAATAGGAATCAGTTTGTC 3' Rev 5' TACTGGAGCCTCTGGTATGG 3'
Sequence based reagent	Rims3 PCR primers (mmu)		PCR primers	FW 5' GCATCAGCGGTGAGATCTGT 3' Rev 5' CTGGGTCAAGCCGACGATAG 3'

363

FISH probe	Mir-138 (Fast Red)	Thermo-Fisher	VM1-10093-VCP	
FISH probe	ErbB4 (488)	Thermo-Fisher	VC4-3146482-VC	
Fish probe	Rims3 (488)	Thermo-Fisher	VC4-3146880-VCP	
FISH probe	Camk2a (488)	Thermo-Fisher	VC6-11639-VCP	
FISH probe	Gad2 (647)	Thermo-Fisher	VC6-16451-VCP	
Antibody	aGAD65+67 (rabbit)	Abcam	Ab11070	1:100 (in vitro); 1:1000 (ex vivo)
Antibody	aMAP2 (Mouse)	Sigma-Aldrich	M9942	1:1000
Antibody	aGFAP (rabbit)	Dako	Z0334	1:1000
Antibody	aParvalbumin (mouse)	SWANT	235	1:1000

Antibody	aVGAT (rabbit)	Synaptic systems	131003	1:1000
Antibody	amCherry (rabbit)	Abcam	Ab167453	1:1000
Antibody	aBeta galatosidase (chicken)	Abcam	Ab9361	1:4000
Antibody	aMouse Alexa Fluor 488 (Donkey)	Invitrogen	A21202	1:500
Antibody	aRabbit Alexa Fluor 546 (Goat)	Invitrogen	A11010	1:500
Antibody	aChicken Alexa Fluor 546 (Goat)	Invitrogen	A11040	1:500
Antibody	aMouse Alexa Fluor 647 (Donkey)	Invitrogen	A31571	1:500
Staining reagent	Hoechst 33342	Thermo Fisher	62249	

364
365
366 **Construct design and cloning**
367
368 *MiR-138 sponge:*
369 MiR-138 sponge was cloned into the BsrGI and HindIII restriction sites of a modified
370 pAAV-6P-SEWB backbone, where the GFP has previously been replaced with
371 dsRed(Christensen et al., 2010). Different number of binding sites were tested, and
372 the plasmid containing 6 binding sites was chosen for further experiments which
373 included the virus production for the creation of the mouse lines.

374 *MiR-138 sponge imperfect binding site*: 5' CGGCCTGATTCGTTCACCAGT 3';
375 spacer sequence: 5' TTTTT 3'; *Control sponge sequence*: 5'
376 TGTGACTGGGGGCCAGAGG 3'; spacer sequence: 5' CAGTG 3'
377
378 AAV-Dlx5/6-miR-138 sponge:
379 Dlx-138-sponge and Dlx-control-sponge were cloned into a modified mCaMKIIα-
380 mCherry-WPRE-hGHp(A) (p199, Viral vector facility of the Neuroscience Center
381 Zurich) backbone where 138-sponge and 138-sponge reversed (control-sponge)
382 were previously inserted using MiR-138 sponge vector as template. The backbone
383 was opened with MluI (NEB: R0198S) and KpnI (NEB: R0142). pAAV-mDlx-GFP-
384 Fishell-1 (gift from Gordon Fishell; Addgene plasmid # 83900) was used to cut out
385 Dlx enhancer and HBB promoter with MluI and EheI (NEB: R0606S).
386 Primers for 138 and control sponge: 5' CACCACCTGTTCCTGTAGTGTAC 3'; 5'
387 CCAGAGGTTGATTATCGATAAGCTTAAC 3'.
388
389 AAV-CMV-Cre:
390 AAV expressing Cre-recombinase under the control of the CMV promoter (gift from
391 Fred Gage; Addgene plasmid #49056).
392
393 *pGL3-138 perfect binding site (pbds) vector:*
394 The oligonucleotides were designed without any specific overhangs to allow blunt
395 end cloning in both directions for a perfect binding site reporter and an antisense
396 control reporter. They were annealed and ligated into a pGL3 promotor vector
397 (Promega, Mannheim) expressing firefly luciferase. For cloning, the pGL3 vector was
398 before digested with XbaI and the ends were blunted to insert the binding sites via
399 blunt end cloning at the 3'end of the firefly open reading frame (ORF). After cloning,
400 several clones were sequenced to determine sense- and antisense reporter.
401 *138 pbds reporter FW:*
402 5'CTAGACGGCCTGATTCACAACACCAGCTACCGGCCTGATTCACAACACCAGC
403 TGGATCC 3'
404 *138 pbds reporter REV:*
405 5'CTAGCGGATCCAGCTGGTGTTGTGAATCAGGCCGGTAGCTGGTGTTGTGAAT
406 CAGGCCGT 3'
407

408 *AAV-miR-138 dual sensor construct*

409 An EcoR1-BglII PCR fragment spanning the pCMV promoter, mCherry coding
410 sequence and SV40 poly adenylation signal was amplified using C1-mCherry
411 (Addgene, 632524) as template. The PCR product was cloned into the BGIII/EcoR1
412 sites of the AAV-hSyn-EGFP (Addgene, 114213), upstream of the human Synapsin
413 1 promoter. Two miR-138 perfectly complementary binding sites were cloned into the
414 SpeI and HIndIII restriction sites, between the EGFP coding sequence and WPRE
415 element of AAV-hSYN-GFP, to generate the final AAV-138 sensor:

416 *138 perfect binding sites FW:*

417 5'CTAGACGGCCTGATTCACAACACCAGCTACCGGCCTGATTCACAACACCAGC
418 TGGATCC 3'

419 *138 perfect binding site REV:*

420 5'CTAGCGGATCCAGCTGGTGTTGTGAATCAGGCCGGTAGCTGGTGTTGTGAAT
421 CAGGCCGT 3'

422 *Luciferase constructs:*

423 pmirGLO dual-luciferase expression vector reporter (Promega, Madison, WI, USA)
424 was used to clone portions of 3' untranslated regions of the investigated mRNAs.
425 XhoI and SalI restriction enzymes were used.

426 *ErbB4 wild type sequence*:

427 5'TTGAATGAAGCAATATGGAAGCAACCAGCAGATTAACTAATTTAAATACTTC 3';

428 *ErbB4 138-mutant sequence*:

429 5'TTGAATGAAGCAATATGGAAGCAgCatGaAGATTAACTAATTTAAATACTTC 3';

430 *Rims3 wild type sequence*:

431 5'GCCTCAGTCACCAGCTCTGTACCAGCAATACTCACCCCTCCACCTCCCTGACT
432 T 3';

433 *Rims3 138-mutant sequence*:

434 5'GCCTCAGTgAtatcCTCTGTACCAGCAATACTCACCCCTCCACCTCCCTGACTT
435 3';

436

437 **Primary neuronal cell culture**

438 Cultures of dissociated primary cortical and hippocampal neurons from embryonic
439 day 18 (E18) Sprague-Dawley rats (Janvier, France) were prepared and cultured as
440 described previously (Schratt et al., 2006). Animal euthanasia was approved by the
441 local cantonal authorities (ZH196/17).

442

443 **Transfection**

444 Transfection of primary neurons was performed using Lipofectamine 2000
445 (Invitrogen, Karlsruhe). For each well of a 24-well plate a total of 1 ug DNA was
446 mixed with a 1:50 dilution of Lipofectamine in NB/NBP medium. After an incubation
447 of 20 min at room temperature, it was further diluted 1:5 in NB/NBP medium and
448 applied to the cells. Neurons were incubated for 2 h with the mix. A 1:1000 dilution of
449 APV (20mM) in NB+/NBP+ was applied for 45-60 min afterwards before exchanging
450 with NB+/NBP+.

451

452 **Luciferase assay**

453 Luciferase assays were performed using the dual-luciferase reporter assay system
454 on a GloMax R96 Microplate Luminometer (Promega). pmirGLO dual-luciferase
455 expression vector reporter (Promega, Madison, WI, USA) was used to clone portions
456 of 3' untranslated regions of the investigated mRNAs. PcDNA3 was used to balance
457 all amounts to a total of 1 ug DNA per condition.

458

459 **Animal lines**

460 The C57BL/6NTac-*Gt(ROSA)26So* $^{tm2459(LacZ,\ antimir_138)\ Arte}$ (hereafter named "138-
461 floxed") mouse lines was created at TaconicArtemis GmbH (Cologne, Germany).
462 The targeting strategy allowed the generation of a constitutive LacZ-miRNA138
463 Sponge Knock-In (KI) allele in the C57Bl/6 mouse ROSA26 locus via targeted
464 transgenesis. The presence of the loxP-flanked transcriptional STOP cassette is
465 expected to terminate the transcription from the CAG promoter and thus prevent the
466 expression of the NLS-LacZ miRNA138 Sponge cDNA, which allows this line to be
467 used as a control (138-floxed line). The constitutive KI allele was obtained after Cre-
468 mediated removal of the loxP-flanked transcriptional STOP cassette from the
469 conditional KI allele, by crossing the 138-flox line with a B6.C-Tg(CMV-Cre)1Cgn
470 (CMV-CRE) line, which allows the expression of the sponge construct (138-sponge^{ub}
471 mice). In all experiments, heterozygous male mice were used. The 138-sponge^{PV}
472 line was generated by crossing 138-floxed line with a previously characterized
473 B6;129P2-*Pvalb*$^{tm1(cre)Arbr}$/J (PV-CRE) line.

474

475 **Behavioral Experiments**

Animals were housed in groups of 3-5 per cage, with food and water *ad libitum*. All experiments were performed on adult male mice (3-5 months old). The animal house had an inverted light-dark cycle, all testing was done during the dark phase (8 am-8 pm). Mice were handled for 10 minutes for 5 days before the experiments began. All measures were analyzed by Noldus Ethovision xt 14, unless stated differently. During the experimental phase, mice were transported individually and allowed to acclimatize to the experimental room in a holding cage for at least 20 minutes before the beginning of the task. At the end of each experiment they were transported back into the animal storage room in their holding cage and placed back into their original home cage with their littermates. 10ml/l detergent (For, Dr .Schnell AG) was used to clean equipment in between trials. Tasks which required the use of the same apparatus were scheduled at least 4 days apart. Two separate cohorts of mice were tested (7 mice each). No cohort-specific differences were found. The behavioral essays were performed from the least to the most stressful: home cage activity, open field, y maze, elevated plus maze, Novel object recognition, contextual fear conditioning. All animal experiments were performed in accordance with the animal protection law of Switzerland and were approved by the local cantonal authorities (ZH017/18).

Open field (OFT):

OFT was performed as described previously (Lackinger et al., 2019). Each session lasted 30 minutes.

Y maze:

Spontaneous alternation: mice were placed in a Y shaped maze (8.5cm width x 50cm length x 10cm height) for 5 minutes. They were free to explore the whole maze and the alternation between the arms was calculated. Novelty preference test: mice were given 5 minutes to explore 2 arms of the maze during the familiarization phase. A door made from the same Plexiglas used for the walls was used to prevent the access of the subjects into the third arm. At the end of the familiarization phase, mice were placed in their holding cage for 90 seconds, while the apparatus was cleaned to avoid olfactory trails. Mice were then placed back into the maze for the test phase, where all three arms where accessible. Preference ratio between the familiar and new arm was then scored based on the time spent in those arms.

Elevated Plus Maze:

510 The maze was elevated 60 cm from the floor, with two arms enclosed by dark
511 Plexiglas walls (5cm width × 30cm length × 15cm height), two opposing open arms
512 and a central platform/intersection. Experiments were conducted in a homogenously
513 illuminated room, with the maze placed in the center of the room. Mice were placed
514 in the central platform of the elevated plus maze. The position and motion of the
515 animals was automatically determined and recorded for 5 min. Time spent and
516 distance travelled in the different arms was scored.
517 *Novel Object Recognition:*
518 Objects were based on the Nature protocol published previously (Leger et al., 2013).
519 They were tested beforehand to assess that no object was preferred, and they were
520 randomized between trials and genotypes. Subjects were placed in the open field
521 arena with two items of the same objects for a 5 min familiarization period. After a 90
522 seconds break in their holding cage while the arena and the objects were cleaned
523 and one object changed, the mice were put back in the arena for the test phase for 5
524 minutes. Time spent exploring the new object was scored manually. Scoring took
525 into consideration the time spent exploring the two objects and the number of visits
526 (nose of the experimental mouse within a 3cm radius from the object).
527 *Contextual Fear Conditioning*
528 This task was performed as previously described (Siegert et al., 2015). Briefly, mice
529 were placed in the open field arena with Plexiglas walls and a metal grid bottom
530 inside the multiconditioning chambers and a metal grid bottom (TSE fear
531 conditioning system, TSE Systems, Germany). They were habituated for 3 min, then
532 foot-shocked (2 s, 0.8 mA constant current) and returned to their home cages. After
533 24 h, mice were placed in the conditioning chamber. Freezing, defined as a total lack
534 of movement except for heartbeat and respiration, was scored for a 3 min period.
535
536 **RNAseq**
537 *RNA extraction* Adult male mice (4 months old) were anaesthetized with isoflurane
538 (Baxter, Unterschleißheim, Germany) and then quickly cervically dislocated and
539 decapitated. Hippocampal tissue was dissected and freshly processed (RNA was
540 extracted using mirVana microRNA Isolation Kit (Life Technologies) according to the
541 manufacturer's instructions.
542 Stranded polyA+ enriched RNA sequencing libraries were prepared at the
543 GENCORE (EMBL, Genomics Core Facility, Heidelberg, Germany) and sequenced

544 on an Illumina HiSeq 2000 machine using a 50nt paired-end protocol (Lackinger et
545 al., 2019).
546 We removed sequencing adapter and quality-trimmed all short reads from the 3'end
547 using FLEXBAR 2.5.3 and a Phred score cutoff >10. All reads longer than 18bp were
548 retained and rRNA reads were subtracted in silico using bowtie2 and an index of the
549 complete repeating rRNA unit (BK000964.3). We used the STAR aligner 2.4.2a4 to
550 map against the mouse genome (EnsEMBL 79 genome + annotations). We
551 performed
552 differential gene expression analysis using Cuffdiff 2.2.1.
553
554 **Quantitative real-time PCR**
555 qPCR was performed as described earlier (Valluy et al., 2015). Primer sequences
556 are given below.
557 ErbB4 FW: 5'GACTCCAATAGGAATCAGTTTGTC 3'
558 ErbB4 REV: 5' TACTGGAGCCTCTGGTATGG 3'
559 Rims3 FW: 5' GCATCAGCGGTGAGATCTGT 3'
560 Rims3 REV: 5' CTGGGTCAAGCCGACGATAG 3'
561
562 **Imaging:**
563 Image acquisition was done with the experimenter being blinded to the different
564 conditions. Pictures were taken on a confocal laser scanning microscope equipped
565 with an Airyscan detector (LSM880, Zeiss). Image analysis was carried out on Fiji
566 (ImageJ).
567 *PV bouton count*: a 63x oil objective was used to take images from CA1
568 hippocampal region immunostained with PV, VGAT and Hoechst was used to
569 counterstain the nuclei (further details in the immunostaining section). The number of
570 PV+ and VGAT+ en passant boutons around the nuclear perimeter were counted
571 and normalized to the total length of the perimeter.
572 vGAT puncta mean intensity:
573 vGAT puncta mean intensity: ImageJ was used to measure the intensity of all the
574 vGAT puncta in the pictures used to quantify PV boutons.
575
576 *PV cell quantification*: a 20x objective was used and PV+ cells were counted on a
577 maximum projection intensity of the CA1 region immunostained with PV (Hoechst

578 was used to counterstain nuclei; further details in the immunostaining section). The
579 number of PV+ cells was normalized to a defined region of interest (230μm x
580 460μm).
581 *Viral mir-138 sensor*: tilescans were taken with a 20x objective of the infected
582 hippocampal region. Intensity of GFP signal was normalized on the mCherry signal
583 per cell. For the analysis, either all neurons (Fig. 1b) or only PV+ neurons (suppl.
584 Fig. 4d) within the CA1 region were taken into consideration.
585
586 **Spine analysis**
587 *In vitro*: Hippocampal neurons were transfected at DIV 10 with 200 ng of GFP and
588 the indicated amount of either miR-138-6x-sponge, CTR sponge, AAV backbone or
589 the Cholesterol-modified 2'O-Me-oligonucleotides ('antagomirs', Thermo Scientific,
590 Karlsruhe. To balance all amounts to a total of 1 ug DNA per condition, PcDNA3 was
591 used. At 18 DIV Cells were fixed using 4 % PFA for 15 min and mounted on glass
592 slides using Aqua-Poly/Mount (Polysciences Inc., Eppelheim). The experimenter was
593 blinded to all the conditions. The z-stack images of GFP-positive neurons exhibiting
594 pyramidal morphology were taken with the 63x objective of a confocal laser scanning
595 microscope (Carl Zeiss, Jena). Eight consecutive optical sections of the dendrites
596 were taken at a 0.4 μm interval with a 1024 x 1024 pixel resolution. Spine volumes
597 were analyzed with the ImageJ software using the maximum intensity projections of
598 the z-stack images. The GFP intensity of 150-200 spines per cell was measured and
599 normalized to the total intensity of the dendritic tree. For each experimental
600 condition, at least 18 representative neurons derived from three independent
601 experiments were analyzed.
602 *In vivo:* brains from 3 months old 138-floxed and 138-sponge^{ub} mice were processed
603 with FD Rapid GolgiStain Kit (Gentaur GmbH, PK401) according to the
604 manufacturer's protocol. Pictures were taken with a Zeiss axio-observer 7 inverted
605 wide field fluorescence microscope equipped with a Axiocam 702 mono Zeiss
606 camera with an 100x oil objective. Dendritic spines were manually analyzed with Fiji
607 (ImageJ).
608
609 **Electrophysiology.**

610 Hippocampal slices (300 µm thick) were prepared at 4 °C, as previously described
611 (Winterer et al., 2019), from 138-floxed, 138-sponge^{ub} and 138-sponge^{PV} mice (age:
612 6-8 weeks) and incubated at 34°C in sucrose-containing artificial cerebrospinal fluid
613 (sucrose-ACSF, in mM: 85 NaCl, 75 sucrose, 2.5 KCl, 25 glucose, 1.25 NaH2PO4, 4
614 MgCl2, 0.5 CaCl2, and 24 NaHCO3) for 0.5 h, and then held at room temperature
615 until recording.
616 Whole cell patch clamp recordings were performed at 32 °C on an upright
617 microscope (Olympus BX51WI) under visual control using infrared differential
618 interference contrast optics. Data were collected with an Axon MultiClamp 700B
619 amplifier and an Digidata 1550B digitizer and analyzed with pClamp 11 software (all
620 from Molecular Devices). Signals were filtered at 2 kHz for miniature EPSCs and
621 miniature IPSCs and digitized at 5 kHz. Stimulus evoked and unitary postsynaptic
622 currents were filtered at 4 kHz, fast-spiking interneurons at 10 kHz, both were
623 digitized at 100 kHz. Recording pipettes were pulled from borosilicate capillary glass
624 (Harvard Apparatus; GC150F-10) with a DMZ-Universal-Electrode-Puller (Zeitz) and
625 had resistances between 2 and 3 MΩ.
626 The extracellular solution (ACSF) was composed of (in mM) 126 NaCl, 2.5 KCl, 26
627 $NaHCO_3$, 1.25 NaH_2PO_4, 2 $CaCl_2$, 2 $MgCl_2$ and 10 glucose. For excitatory
628 postsynaptic currents (EPSCs) measured in CA1 pyramidal cells and for fast-spiking
629 interneurons the intracellular solution was composed of 125 K-Gluconate, 20 KCl 0.5
630 EGTA, 10 HEPES, 4 Mg-ATP, 0.3 GTP and 10 Na_2-phosphocreatine (adjusted to pH
631 7.3 with KOH). Cells were held at -70mV for miniature EPSC (mEPSCs) and at -
632 60mV for stimulus evoked excitatory postsynaptic currents (eEPSCs). 1µM Gabazine
633 was added to isolate AMPA-mediated postsynaptic currents, additionally 1µM TTX
634 for mEPSCs. For inhibitory postsynaptic currents (IPSCs) intracellular solution was
635 composed of 135 Cs-Gluconate, 5 KCl, 2 NaCl, 0.2 EGTA, 10 HEPES, 4 Mg-ATP,
636 0.3 GTP and 10 Na_2-phosphocreatine (adjusted to pH 7.3 with CsOH). Cells were
637 held at +10mV for miniature IPSC (mIPSCs) and at -10mV for stimulus evoked and
638 unitary inhibitory postsynaptic currents (eIPSCs and uIPSCs). 25µM AP-5, 10µM
639 NBQX and 10µM SCH 50911 were added to isolate GABAa-mediated postsynaptic
640 currents for eIPSCs, additionally 1µM TTX for mIPSCs. Synaptic currents were
641 evoked by mono-polar stimulation with a patch pipette filled with ACSF and
642 positioned in the middle of CA1 stratum radiatum for eEPSCs and in stratum
643 pyramidale for eIPSCs. Series resistance of CA1 pyramidal neurons (not

644 compensated; range, from 7.0 to 19.7 MΩ; median, 11.3 MΩ; IQR, 2.4 MΩ) was
645 monitored and recordings were discarded if series resistance changed by more than
646 20%. Membrane potentials were not corrected for liquid junction potential.
647
648 For paired recordings, whole cell configuration was first established in putative fast-
649 spiking interneurons. Cells were selected based on morphological appearance in
650 stratum pyramidale of hippocampal CA1, on fast-spiking properties and on input
651 resistance characteristic for PV-positive interneurons (Que et al., 2021)(**suppl. Fig.**
652 **6f**). Subsequently whole cell recordings were made from postsynaptic CA1
653 pyramidal neurons residing in close proximity to the presynaptic fast-spiking
654 interneuron. Presynaptic fast-spiking interneurons were held in current-clamp mode
655 and series resistance was compensated with the automatic bridge balance of the
656 amplifier. The mean resting potential of the presynaptic fast-spiking interneurons was
657 -65 ± 4.1mV (mean ± sd; **suppl. Fig. 6f)**. Fast-spiking interneurons were stimulated
658 at 1Hz for uIPSCs and at 0.03Hz for paired pulse uIPSCs. To characterize the
659 discharge behavior of fast-spiking interneurons, depolarizing steps (50pA) of 1500ms
660 were applied. The spiking frequency (**suppl. Fig. 6f**) was determined at 800 to
661 1000pA current injection. Input resistance was calculated from the mean deviation
662 from baseline of steady state voltage responses evoked by -150, -100 and -50 pA
663 current injections.
664
665 **Cell type enrichment analysis**
666 For the cell type enrichment analysis, we used the single-cell data and annotation
667 from Zeisel et al. (2018). We downloaded single-cell count data and annotation from
668 https://storage.googleapis.com/linnarsson-lab-loom/l5_all.loom, restricted it to
669 hippocampus cells, and aggregated to the pseudo-bulk level using muscat (Crowell
670 et al., 2020) and the authors' cell identities. We retained only cell types represented
671 by more than 50 cells, and normalized using TMM (Robinson and Oshlack, 2010).
672 For each gene, we then identified the cell type in which it was the most highly
673 expressed, forming gene sets for each cell type. We then created a sponge
674 differential expression signature by multiplying the sign of the foldchange with the -
675 log10(p-value) of each gene and looked for enrichment of gene sets in this signature
676 using fgsea (Korotkevich et al., Biorxiv 2021, doi: 10.1101/060012).
677

678 **GO enrichment analysis**

679 The R Bioconductor package TopGo (v.2.42.0) was used to perform Gene Ontology
680 enrichment analysis, essentially as in (Lackinger et al., 2019).
681 To sum up, genes were annotated with the "Cellular Component" ontology and
682 significantly changed genes subsequently tested against the expressed background.
683 For the main figure we plotted the Top10 GO-Terms ranked by significance (filtering
684 out those with more than 200 annotated genes).
685

686 **miRNA binding site analysis**

687 Mouse 3'UTR positions of predicted conserved microRNA binding sites were
688 downloaded from Targetscan (version 7.2)(Agarwal et al., 2015) and filtered for the
689 seed of miR-138-5p. Putative miR-138 targets (including site-type information) were
690 then aligned with the genes and log fold changes (logFC) as obtained by the
691 differential expression analysis. Plotted is the cumulative proportion (logFC rank (-1)
692 / number of genes (-1)) over the logFC.
693

694 **Single-molecule fluorescence *in situ* hybridization (smFISH)**

695 smFISH for miRNA detection on hippocampal neuron cultures was performed using
696 the QuantiGene ViewRNA miRNA Cell Assay kit (Thermo Fisher) according to the
697 manufacturer's protocol with slight modifications. To preserve dendrite morphology,
698 protease treatment was reduced to a dilution of 1:10,000 in PBS for 45 sec. smFISH
699 for mRNA detection was performed using the QuantiGene ViewRNA ISH Cell Assay
700 kit (Thermo Fisher) as previously described (Valluy et al., 2015), but omitting the
701 protease treatment. After completion of the FISH protocol, cells were washed with
702 PBS, pre-blocked in gelatin detergent buffer and processed for immunostaining.
703 Pictures represent maximum intensity projections of z-stack images taken on a
704 confocal laser scanning microscope equipped with an Airyscan detector (LSM880,
705 Zeiss).
706

707 **Stereotactic surgery**

708 The viral vector (aaAAV-9/2 [hCMV-mCherry-SV40p(A)]rev-hSyn1-EGFP-2x (miR-
709 138-5p)-WPRE-SV40p(A)) was produced by the local Viral Vector Facility (VVF9 of
710 the Neuroscience Center Zurich). The produced virus had a physical titer of 6.1
711 x10e^{12} vector genomes/ml. Stereotactic brain injections were performed on two- to

712 three-month-old 138-floxed and 138-sponge^{ub} mice as previously described(Zerbi et
713 al., 2019)). Briefly, mice were anesthetized with isoflurane and subsequentially
714 placed onto the stereotaxic frame. Before and after the procedure, animals received
715 subcutaneous injection of 2 mg/kg Meloxicam for analgesia and local anaesthetic
716 (Emla cream 5% lidocaine, 5% prilocaine) was distributed on the head. Animals were
717 injected bilaterally with 1µl of virus into the dorsal hippocampus (coordinates from
718 bregma: anterior/posterior −2.1 mm, medial/lateral ± 1.5 mm, dorsal/ventral
719 −1.8 mm) and 1µl of virus in the ventral hippocampus (coordinates from bregma:
720 anterior/posterior −3.3 mm, medial/lateral ± 2.75 mm, dorsal/ventral −4.0 mm). Post-
721 operative health checks were carried on over the three days after surgery.

722 **Tissue collection**

723 Animals were sacrificed by intraperitoneal injection of pentobarbital (150 mg/kg).
724 When in deep anaesthesia, mice were perfused intracardially with ice-cold PBS pH
725 7.4, followed by perfusion with 4% paraformaldehyde in PBS pH 7.4. The brains
726 were then isolated and postfixed for 2-3h (138-floxed; 138-sponge^{PV} mice) or
727 overnight (138-flox and 138-sponge^{ub} mice) at 4°C. The fixed tissue was placed in
728 sucrose solution (30% sucrose in PBS) for 24h and frozen in tissue mounting
729 medium (OCT mounting media, VWR chemicals). The tissue was coronally
730 sectioned at 50-60µm thickness on a cryostat, immediately placed in ice-cold PBS
731 and subsequentially conserved in cryoprotectant solution (15% glucose, 30%
732 ethylene glycol, 5mM NaH_2PO_4*H_2O, 20mM Na_2HPO_4*$2H_2O$) at -20°C.
733

734 **Immunohistochemistry**

735 Ex *vivo (cryosections)*: For immunofluorescence, cryosections were washed in ice-
736 cold PBS for 30 minutes, placed on microscope slides (Menzel-Gläser
737 SUPERFROST PLUS, Thermo Scientific) and air-dried for 5-10 min. Afterwards,
738 permeabilization was performed by incubating sections in permeabilization solution
739 (0.5% Triton X-100 in PBS) for 30 min at room temperature, followed by a blocking
740 step in blocking buffer (0.5% Triton X-100, 300mM NaCl, 10% Normal Goat Serum in
741 PBS) with addition of blocking Reagent (VC-MKB-2213, Adipogen Life Sciences,
742 1:10 dilution) for 1h at room temperature. Cryosections were washed in PBS twice
743 for 10 min at room temperature and incubated with primary antibodies in blocking
744 buffer overnight at 4°C. Subsequentially, the sections were washed 3 times with

745 blocking buffer, incubated with secondary antibodies and Hoechst 33342 in blocking
746 buffer for 1h at room temperature, washed again three times in blocking buffer,
747 washed in PBS, air-dried and mounted with Aqua-Poly/Mount (POL18606,
748 Polysciences).
749 *Ex vivo (vibratome sections)*: For immunofluorescence, 300µM sections were sliced
750 on a vibratome in ice cold sucrose-containing artificial cerebrospinal fluid, and then
751 fixed in 4% PFA overnight. Free-floating sections were washed in ice-cold 1X PBS
752 for 30min, permeabilized by incubation in 0.5% PBX (0.5% Triton X-100 in PBS) for
753 30 min at room temperature, followed by a quenching step in 0.1M Glycine to reduce
754 background autofluorescence. Sections were blocked in blocking buffer (0.5% PBX,
755 10% normal goat serum in PBS) for 1h at room temperature, and then incubated in
756 primary antibodies for 36 hours at 4°C. Sections were washed in 0.05% PBX twice
757 for 10 min at room temperature, and then incubated with secondary antibodies in
758 0.05% PBX with 10% normal goat serum at room temperature for 3 hours.
759 Subsequentially, the sections were washed 3 times with 0.05% PBX, incubated with
760 Hoechst 33342 in 1X PBS for 10min, and then washed again three times in PBS,
761 mounted on SuperFrost+ slides with Aqua-Poly/Mount (POL18606, Polysciences). A
762 40uM Z-stack (with 0.25uM z-step) was acquired on a Zeiss LSM 880 confocal
763 microscope, with a Plan-Apochromatic 63X/1.4NA DIC M27 oil objective and
764 FastAiryScan detector settings in the hippocampal CA1 region.
765 In *vitro*: cells were washed once with NBP, fixed for 20 minutes with 4%PFA and,
766 after five washes with PBS (3xfast;2x5minutes), permeabilized with GDB (20 mM
767 sodium phosphate buffer (pH 7.4), 450 mM NaCl, 0.3 % Triton X-100, 0.1 % gelatin,
768 ddH_2O)
769 for 20 minutes. Primary antibody was diluted in GDB and incubated for 1h at room
770 temperature, followed by five washes with PBS (3xfast;2x5minutes). Secondary
771 antibody was diluted in GDB and incubated in the dark, at room temperature for 1h.
772 The cells were then washed again with PBS (3xfast;2x5minutes). In the second last
773 wash Hoechst 33342 was added to the PBS. The coverslips were mounted with
774 Aqua-Poly/Mount (POL18606, Polysciences) on microscope slides (Menzel-Gläser
775 SUPERFROST PLUS, Thermo Scientific).
776
777 **Statistics**

Statistical analysis was performed on either GraphPad Prism 8.0 or RStudio. Plots were generated in R, mainly using the packages ggplot2, ggsci, ggrepel and scales. For data sets with n>4, Box plots (Tukey style) were used. For data sets with n<5, average +/- s.d., including individual data points, is shown. Normal distribution of data was tested with the Shapiro-Wilk test. Based on the results, parametric (e.g. Student's t-test) or non-parametric (e.g. Mann-Whitney, Kolmogorov-Smirnov) tests were used.

The detailed parameters (n, p-value, test) for the statistical assessment of the data are provided in the figure legends.

Acknowledgments

We are grateful to S. Brown and M. Müller for valuable comments on the manuscript, T. Wüst and C. Furler for excellent technical assistance, T. Germade for help with bioinformatics, D. Colameo for help with animal perfusions and microscopy data analysis scripts, A. Loye for help with histology and T. Demeter for help with cloning. We thank G. Fishell, F. Gage and the Viral Vector Facility of the Neuroscience Center Zurich for sharing plasmids. This work was supported by grants from the DFG (SCHR 1136/4-2) and the ETH (24 18-2 (NeuroSno).

Data and code availability

RNA-seq data (Fig. 2, suppl. Fig.2) has been deposited to GEO (accession no. GSE173982). Source data are attached as zip folders to the individual figures of the submission.

Competing interests:

The authors declare no competing interests.

References:

Agarwal, V., Bell, G.W., Nam, J.W., and Bartel, D.P. (2015). Predicting effective microRNA target sites in mammalian mRNAs. Elife *4*.

Bartel, D.P. (2018). Metazoan MicroRNAs. Cell *173*, 20-51.

Beveridge, N.J., Gardiner, E., Carroll, A.P., Tooney, P.A., and Cairns, M.J. (2010). Schizophrenia is associated with an increase in cortical microRNA biogenesis. Mol Psychiatry *15*, 1176-1189.

Booker, S.A., and Vida, I. (2018). Morphological diversity and connectivity of hippocampal interneurons. Cell Tissue Res *373*, 619-641.

Boscher, E., Goupil, C., Petry, S., Keraudren, R., Loiselle, A., Planel, E., and Hebert, S.S. (2020). MicroRNA-138 Overexpression Alters Abeta42 Levels and Behavior in Wildtype Mice. Front Neurosci *14*, 591138.

Cheng, Y., Wang, Z.M., Tan, W., Wang, X., Li, Y., Bai, B., Li, Y., Zhang, S.F., Yan, H.L., Chen, Z.L.*, et al.* (2018). Partial loss of psychiatric risk gene Mir137 in mice causes repetitive behavior and impairs sociability and learning via increased Pde10a. Nat Neurosci *21*, 1689-1703.

Christensen, M., Larsen, L.A., Kauppinen, S., and Schratt, G. (2010). Recombinant Adeno-Associated Virus-Mediated microRNA Delivery into the Postnatal Mouse Brain Reveals a Role for miR-134 in Dendritogenesis in Vivo. Frontiers in neural circuits *3*, 16.

Crowell, H.L., Soneson, C., Germain, P.L., Calini, D., Collin, L., Raposo, C., Malhotra, D., and Robinson, M.D. (2020). muscat detects subpopulation-specific state transitions from multi-sample multi-condition single-cell transcriptomics data. Nat Commun *11*, 6077.

Del Pino, I., Rico, B., and Marin, O. (2018). Neural circuit dysfunction in mouse models of neurodevelopmental disorders. Curr Opin Neurobiol *48*, 174-182.

Ebert, M.S., and Sharp, P.A. (2010). MicroRNA sponges: progress and possibilities. Rna *16*, 2043-2050.

Fazzari, P., Paternain, A.V., Valiente, M., Pla, R., Lujan, R., Lloyd, K., Lerma, J., Marin, O., and Rico, B. (2010). Control of cortical GABA circuitry development by Nrg1 and ErbB4 signalling. Nature *464*, 1376-1380.

Fuchs, E.C., Zivkovic, A.R., Cunningham, M.O., Middleton, S., Lebeau, F.E., Bannerman, D.M., Rozov, A., Whittington, M.A., Traub, R.D., Rawlins, J.N.*, et al.* (2007). Recruitment of parvalbumin-positive interneurons determines hippocampal function and associated behavior. Neuron *53*, 591-604.

Gandal, M.J., Zhang, P., Hadjimichael, E., Walker, R.L., Chen, C., Liu, S., Won, H., van Bakel, H., Varghese, M., Wang, Y.*, et al.* (2018). Transcriptome-wide isoform-level dysregulation in ASD, schizophrenia, and bipolar disorder. Science *362*.

Gao, J., Wang, W.Y., Mao, Y.W., Graff, J., Guan, J.S., Pan, L., Mak, G., Kim, D., Su, S.C., and Tsai, L.H. (2010). A novel pathway regulates memory and plasticity via SIRT1 and miR-134. Nature *466*, 1105-1109.

Giusti, S.A., Vogl, A.M., Brockmann, M.M., Vercelli, C.A., Rein, M.L., Trumbach, D., Wurst, W., Cazalla, D., Stein, V., Deussing, J.M.*, et al.* (2014). MicroRNA-9 controls dendritic development by targeting REST. Elife *3*.

Hajos, N., Palhalmi, J., Mann, E.O., Nemeth, B., Paulsen, O., and Freund, T.F. (2004). Spike timing of distinct types of GABAergic interneuron during hippocampal gamma oscillations in vitro. J Neurosci *24*, 9127-9137.

He, M., Liu, Y., Wang, X., Zhang, M.Q., Hannon, G.J., and Huang, Z.J. (2012). Cell-type-based analysis of microRNA profiles in the mouse brain. Neuron *73*, 35-48.

857 Konopka, W., Kiryk, A., Novak, M., Herwerth, M., Parkitna, J.R., Wawrzyniak, M., Kowarsch,
858 A., Michaluk, P., Dzwonek, J., Arnsperger, T.*, et al.* (2010). MicroRNA loss enhances learning
859 and memory in mice. J Neurosci *30*, 14835-14842.
860 Kumar, R.A., Sudi, J., Babatz, T.D., Brune, C.W., Oswald, D., Yen, M., Nowak, N.J., Cook, E.H.,
861 Christian, S.L., and Dobyns, W.B. (2010). A de novo 1p34.2 microdeletion identifies the
862 synaptic vesicle gene RIMS3 as a novel candidate for autism. J Med Genet *47*, 81-90.
863 Lackinger, M., Sungur, A.O., Daswani, R., Soutschek, M., Bicker, S., Stemmler, L., Wust, T.,
864 Fiore, R., Dieterich, C., Schwarting, R.K.*, et al.* (2019). A placental mammal-specific
865 microRNA cluster acts as a natural brake for sociability in mice. EMBO Rep *20*.
866 Leger, M., Quiedeville, A., Bouet, V., Haelewyn, B., Boulouard, M., Schumann-Bard, P., and
867 Freret, T. (2013). Object recognition test in mice. Nat Protoc *8*, 2531-2537.
868 Lovett-Barron, M., Kaifosh, P., Kheirbek, M.A., Danielson, N., Zaremba, J.D., Reardon, T.R.,
869 Turi, G.F., Hen, R., Zemelman, B.V., and Losonczy, A. (2014). Dendritic inhibition in the
870 hippocampus supports fear learning. Science *343*, 857-863.
871 Markram, H., Toledo-Rodriguez, M., Wang, Y., Gupta, A., Silberberg, G., and Wu, C. (2004).
872 Interneurons of the neocortical inhibitory system. Nat Rev Neurosci *5*, 793-807.
873 McNeill, E., and Van Vactor, D. (2012). MicroRNAs shape the neuronal landscape. Neuron
874 *75*, 363-379.
875 Moreau, M.P., Bruse, S.E., David-Rus, R., Buyske, S., and Brzustowicz, L.M. (2011). Altered
876 microRNA expression profiles in postmortem brain samples from individuals with
877 schizophrenia and bipolar disorder. Biological psychiatry *69*, 188-193.
878 Murray, A.J., Sauer, J.F., Riedel, G., McClure, C., Ansel, L., Cheyne, L., Bartos, M., Wisden, W.,
879 and Wulff, P. (2011). Parvalbumin-positive CA1 interneurons are required for spatial
880 working but not for reference memory. Nat Neurosci *14*, 297-299.
881 Nicodemus, K.K., Luna, A., Vakkalanka, R., Goldberg, T., Egan, M., Straub, R.E., and
882 Weinberger, D.R. (2006). Further evidence for association between ErbB4 and schizophrenia
883 and influence on cognitive intermediate phenotypes in healthy controls. Mol Psychiatry *11*,
884 1062-1065.
885 Pelkey, K.A., Chittajallu, R., Craig, M.T., Tricoire, L., Wester, J.C., and McBain, C.J. (2017).
886 Hippocampal GABAergic Inhibitory Interneurons. Physiological reviews *97*, 1619-1747.
887 Pouille, F., and Scanziani, M. (2001). Enforcement of temporal fidelity in pyramidal cells by
888 somatic feed-forward inhibition. Science *293*, 1159-1163.
889 Qiu, F., Mao, X., Liu, P., Wu, J., Zhang, Y., Sun, D., Zhu, Y., Gong, L., Shao, M., Fan, K.*, et al.*
890 (2020). microRNA Deficiency in VIP+ Interneurons Leads to Cortical Circuit Dysfunction.
891 Cereb Cortex *30*, 2229-2249.
892 Que, L., Lukacsovich, D., Luo, W., and Foldy, C. (2021). Transcriptional and morphological
893 profiling of parvalbumin interneuron subpopulations in the mouse hippocampus. Nat
894 Commun *12*, 108.
895 Rico, B., and Marin, O. (2011). Neuregulin signaling, cortical circuitry development and
896 schizophrenia. Curr Opin Genet Dev *21*, 262-270.
897 Robinson, M.D., and Oshlack, A. (2010). A scaling normalization method for differential
898 expression analysis of RNA-seq data. Genome Biol *11*, R25.
899 Sakamoto, H., Ariyoshi, T., Kimpara, N., Sugao, K., Taiko, I., Takikawa, K., Asanuma, D.,
900 Namiki, S., and Hirose, K. (2018). Synaptic weight set by Munc13-1 supramolecular
901 assemblies. Nat Neurosci *21*, 41-49.
902 Schratt, G. (2009). microRNAs at the synapse. Nat Rev Neurosci *10*, 842-849.

903 Schratt, G.M., Tuebing, F., Nigh, E.A., Kane, C.G., Sabatini, M.E., Kiebler, M., and Greenberg,
904 M.E. (2006). A brain-specific microRNA regulates dendritic spine development. Nature *439*,
905 283-289.
906 Schroder, J., Ansaloni, S., Schilling, M., Liu, T., Radke, J., Jaedicke, M., Schjeide, B.M.,
907 Mashychev, A., Tegeler, C., Radbruch, H.*, et al.* (2014). MicroRNA-138 is a potential
908 regulator of memory performance in humans. Front Hum Neurosci *8*, 501.
909 Siegel, G., Obernosterer, G., Fiore, R., Oehmen, M., Bicker, S., Christensen, M.,
910 Khudayberdiev, S., Leuschner, P.F., Busch, C.J., Kane, C.*, et al.* (2009). A functional screen
911 implicates microRNA-138-dependent regulation of the depalmitoylation enzyme APT1 in
912 dendritic spine morphogenesis. Nat Cell Biol *11*, 705-716.
913 Siegert, S., Seo, J., Kwon, E.J., Rudenko, A., Cho, S., Wang, W., Flood, Z., Martorell, A.J.,
914 Ericsson, M., Mungenast, A.E.*, et al.* (2015). The schizophrenia risk gene product miR-137
915 alters presynaptic plasticity. Nat Neurosci *18*, 1008-1016.
916 Sohal, V.S., and Rubenstein, J.L.R. (2019). Excitation-inhibition balance as a framework for
917 investigating mechanisms in neuropsychiatric disorders. Mol Psychiatry *24*, 1248-1257.
918 Takada, Y., Hirano, M., Kiyonaka, S., Ueda, Y., Yamaguchi, K., Nakahara, K., Mori, M.X., and
919 Mori, Y. (2015). Rab3 interacting molecule 3 mutations associated with autism alter
920 regulation of voltage-dependent Ca(2)(+) channels. Cell Calcium *58*, 296-306.
921 Tan, C.L., Plotkin, J.L., Veno, M.T., von Schimmelmann, M., Feinberg, P., Mann, S., Handler,
922 A., Kjems, J., Surmeier, D.J., O'Carroll, D.*, et al.* (2013). MicroRNA-128 governs neuronal
923 excitability and motor behavior in mice. Science *342*, 1254-1258.
924 Tatro, E.T., Risbrough, V., Soontornniyomkij, B., Young, J., Shumaker-Armstrong, S., Jeste,
925 D.V., and Achim, C.L. (2013). Short-term recognition memory correlates with regional CNS
926 expression of microRNA-138 in mice. Am J Geriatr Psychiatry *21*, 461-473.
927 Tian, F., Yuan, C., and Yue, H. (2018). MiR-138/SIRT1 axis is implicated in impaired learning
928 and memory abilities of cerebral ischemia/reperfusion injured rats. Exp Cell Res *367*, 232-
929 240.
930 Tian, J., Geng, F., Gao, F., Chen, Y.H., Liu, J.H., Wu, J.L., Lan, Y.J., Zeng, Y.N., Li, X.W., Yang,
931 J.M.*, et al.* (2017). Down-Regulation of Neuregulin1/ErbB4 Signaling in the Hippocampus Is
932 Critical for Learning and Memory. Molecular neurobiology *54*, 3976-3987.
933 Tuncdemir, S.N., Fishell, G., and Batista-Brito, R. (2015). miRNAs are Essential for the
934 Survival and Maturation of Cortical Interneurons. Cereb Cortex *25*, 1842-1857.
935 Valluy, J., Bicker, S., Aksoy-Aksel, A., Lackinger, M., Sumer, S., Fiore, R., Wust, T., Seffer, D.,
936 Metge, F., Dieterich, C.*, et al.* (2015). A coding-independent function of an alternative Ube3a
937 transcript during neuronal development. Nat Neurosci *18*, 666-673.
938 Walgrave, H., Balusu, S., Snoeck, S., Vanden Eynden, E., Craessaerts, K., Thrupp, N., Wolfs, L.,
939 Horre, K., Fourne, Y., Ronisz, A.*, et al.* (2021). Restoring miR-132 expression rescues adult
940 hippocampal neurogenesis and memory deficits in Alzheimer's disease. Cell Stem Cell *28*,
941 1805-1821 e1808.
942 Wang, H., Liu, F., Chen, W., Sun, X., Cui, W., Dong, Z., Zhao, K., Zhang, H., Li, H., Xing, G.*, et*
943 *al.* (2018). Genetic recovery of ErbB4 in adulthood partially restores brain functions in null
944 mice. Proc Natl Acad Sci U S A *115*, 13105-13110.
945 Watanabe, Y., Shibuya, M., Nunokawa, A., Kaneko, N., Igeta, H., Egawa, J., Someya, T.,
946 Hishimoto, A., Mouri, K., and Sora, I. (2014). A rare MIR138-2 gene variation is associated
947 with schizophrenia in a Japanese population. Psychiatry Res *215*, 801-802.

Wen, L., Lu, Y.S., Zhu, X.H., Li, X.M., Woo, R.S., Chen, Y.J., Yin, D.M., Lai, C., Terry, A.V., Jr., Vazdarjanova, A.*, et al.* (2010). Neuregulin 1 regulates pyramidal neuron activity via ErbB4 in parvalbumin-positive interneurons. Proc Natl Acad Sci U S A *107*, 1211-1216.

Winterer, J., Lukacsovich, D., Que, L., Sartori, A.M., Luo, W., and Foldy, C. (2019). Single-cell RNA-Seq characterization of anatomically identified OLM interneurons in different transgenic mouse lines. Eur J Neurosci *50*, 3750-3771.

Zeisel, A., Hochgerner, H., Lonnerberg, P., Johnsson, A., Memic, F., van der Zwan, J., Haring, M., Braun, E., Borm, L.E., La Manno, G.*, et al.* (2018). Molecular Architecture of the Mouse Nervous System. Cell *174*, 999-1014 e1022.

Zerbi, V., Floriou-Servou, A., Markicevic, M., Vermeiren, Y., Sturman, O., Privitera, M., von Ziegler, L., Ferrari, K.D., Weber, B., De Deyn, P.P.*, et al.* (2019). Rapid Reconfiguration of the Functional Connectome after Chemogenetic Locus Coeruleus Activation. Neuron *103*, 702-718 e705.

964 **Figure legends**

965

966 **Figure 1**

967 **(a)** Schematic overview of the strategy for generating 138-sponge^{ub} mice. **(b)** Left:
968 representative images of mCherry and GFP expression in hippocampal neurons
969 from 138-floxed and 138-sponge^{ub} mice, respectively. Right: bar graphs of
970 GFP/mCherry ratios from CA1 hippocampal neurons infected with a 138-pbds
971 sensor construct; 138-floxed: n=105 cells from two mice, 138-sponge^{ub}: n=127cells
972 from three mice; p= 0.02 (KS-test). **(c)** Upper panel: schematic representation of the
973 Y maze novelty preference task; lower panel: exploration time spent in familiar (F)
974 and novel (N) arm; 138-floxed n=12 mice; 138-sponge^{ub} n=14 mice; ***p=0.005;
975 n.s.=0.711 (Student's two-tailed heteroscedastic t test). **(d)** Upper panel: schematic
976 representation of the novel object recognition task; lower panel: exploration time
977 presented as percentage of total time spent with either novel or familiar object; 138-
978 floxed n=12 mice; 138-sponge^{ub} n=12 mice; **** p<0.00002; n.s. p=0.11 (Student's
979 two tailed heteroscedastic t test). **(e)** Upper: schematic representation of the
980 contextual fear conditioning task; lower: time (s) mice spent freezing 24 h after the
981 foot shock was administrated; 138-floxed n=7 mice; 138-sponge^{ub} n=7 mice; n.s.
982 p=0.97 (Student's two-tailed heteroscedastic t test). **(f)** mEPSC recording in CA1
983 pyramidal neurons. Upper panel: example traces; scale bar: 20 pA, 500 ms. Lower
984 panel left: mEPSC amplitude (138-floxed: range, from 14.3 to 25.6 pA; median, 17.2
985 pA; interquartile range [IQR], 3.9 pA. 138-sponge^{ub}: range, from 14.1 to 25.2 pA;
986 median, 17.4 pA; IQR, 3.1 pA; n.s. p=0.74 Student's two-tailed heteroscedastic t
987 test). Lower panel right: mEPSC frequency (138-floxed: range, from 0.2 to 0.9 Hz;
988 median, 0.5 Hz; IQR, 0.2 Hz. 138-sponge^{ub}: range, from 0.3 to 0.7 Hz; median, 0.5
989 Hz; IQR, 0.1 Hz; n.s. p=0.91 Student's two-tailed heteroscedastic t test). 138-floxed
990 n=13 cells/4mice; 138-sponge^{ub} n=13cells/3mice. **(g)** Upper panel: representative
991 images of Golgi-stained CA1 pyramidal neuron dendritic segments of the indicated
992 genotypes. Lower panel: quantification of dendritic spine width (left) and density
993 (number/μm; right) based on Golgi staining; 138-floxed: n=15 cells from 3 mice
994 (1312 spines total); 138-sponge^{ub} n=18 cells from 3 mice (1687 spines total) (n.s.,
995 p=0.25 (width); p=0.49 (density); Student's two tailed heteroscedastic t test).

996 **Figure 1 – source data:** this file contains the raw data on which the graphs in Fig. 1
997 are based.
998
999
1000
1001 **Figure 2**
1002 **(a)** Volcano plot of differentially expressed genes (DEGs) obtained from polyA-
1003 RNAseq of total hippocampal RNA from 138-flox and 138-sponge^{ub} mice. N=3.
1004 Genes with FDR<0.05 are labeled blue (downregulated) or green (upregulated).
1005 Rims3 and Erbb4 are indicated. **(b)** Cumulative distribution plots of log_2-fold
1006 expression changes (138-sponge^{ub}/138-floxed) for genes either containing (targets,
1007 red curve) or not containing (non-targets, black curve) predicted miR-138 binding
1008 sites. p=2.55e^{-05} (KS-test). **(c)** Gene ontology (GO) term analysis for DEGs. Top ten
1009 enriched cellular component (CC) GO terms with less than 200 total genes are
1010 shown. **(d)** Enrichment analysis of DEGs in different brain cell types based on
1011 published single-cell RNA-seq data(Zeisel et al., 2018). Normalized enrichment
1012 score>0: upregulated in 138-sponge^{ub} mice.
1013
1014 **Figure 3**
1015 **(a)** Single-molecule (Sm) FISH analysis of miR-138 (red) together with Camk2a or
1016 Erbb4 mRNA to label excitatory or inhibitory neurons, respectively. Hoechst was
1017 used to counterstain nuclei. GAD65/67 antibody staining was used to identify
1018 GABAergic neurons. Scale bar=100μm (upper); 20μm (lower left and center), 5μm
1019 (lower right). **(b)** qPCR analysis of ErbB4 mRNA in total hippocampal RNA obtained
1020 from 138-floxed or 138-sponge^{ub} mice. U6 snRNA was used for normalization. n=3
1021 mice; *p=0.003, (Student's two-tailed heteroscedastic t test) **(c, d)** Western blot
1022 analysis of Erbb4 protein in hippocampal lysates from 138-floxed or 138-sponge^{ub}
1023 mice (c) or lysates from rat hippocampal neurons (DIV12) transfected with miR-138
1024 or control mimic (d). Tubulin was used for normalization. (c) n=3 mice; *p=0.025
1025 (student's two-tailed heteroscedastic t test); (d) n=3 independent transfections;
1026 ***p=0.0009 (one sample t-test). **(e)** Relative luciferase activity in rat cortical neurons
1027 (DIV9-12) transfected with Erbb4 3'UTR constructs with (138mut) or without (wt) a
1028 mutation in the miR-138 binding site, together with miR-138 or negative control

1029 mimics. Negative control mimic = 1. n=4 independent transfections, *p=0.025, n.s.
1030 p= 0.09 (student's two-tailed heteroscedastic t test). **(f)** Sm FISH analysis of Erbb4
1031 (green) in rat hippocampal interneurons infected with Dlx-control-sponge or miR-138-
1032 sponge. Left panel: representative neurons, scale bar=20 μm. Green: Erbb4 FISH;
1033 grey: DAPI (nuclei); red: mCherry (Dlx5/6 expressing interneurons). Right panel:
1034 Erbb4 FISH quantification. Control sponge=1. N=3 independent infections (10-12
1035 cells per condition), ***p=0.0004 (one-sample t-test).
1036 **Figure 3 – source data:** this file contains the raw data on which the graphs in Fig. 3
1037 are based.
1038
1039 **Figure 4**
1040 **(a)** Representative pictures of hippocampal interneurons *in vivo* infected with rAAV-
1041 Dlx-138-sponge. Upper panel: infected interneurons in hippocampal area CA1. Scale
1042 bar=50 μm. Middle and lower panel: neurons in hippocampal area CA1 at higher
1043 magnification. Left neuron: infected with rAAV-Dlx-138-sponge, expressing
1044 GAD65/67; right neuron: not infected, no GAD65/67 expression. Scale bar=10 μm.
1045 red: mCherry; grey: GAD65/67, blue: Hoechst nuclei. **(b)** Upper panel: schematic
1046 representation of the Y maze novelty preference task; lower panel: exploration time
1047 spent in familiar (F) and novel (N) arm; Dlx-control sponge n=8 mice; Dlx-miR-138
1048 sponge n=9 mice; ****p=0.00005; n.s.=0.079 (Student's two-tailed heteroscedastic t
1049 test). **(c)** Upper panel: schematic representation of the novel object recognition task;
1050 lower panel: exploration time presented as percentage of total time spent with either
1051 novel or familiar object; Dlx-control sponge n=9 mice; Dlx-miR-138 sponge n=10
1052 mice; *p=0.03; n.s.=0.33 (Student's two tailed heteroscedastic t test). **(d)** mIPSC
1053 frequency in CA1 pyramidal neurons. Upper panel left: example traces, Dlx-control
1054 sponge in orange, Dlx-miR-138 sponge in purple, scale bar: 50 pA, 200 ms. Lower
1055 panel left: mIPSC frequency (Dlx-control sponge: range, from 2.0 to 7.1 Hz; median,
1056 3.8 Hz; IQR, 1.3 Hz. Dlx-miR-138 sponge: range, from 3.2 to 11.3 Hz; median, 6.4
1057 Hz; IQR, 4.0 Hz; ****p < 0.0001, Student's two-tailed heteroscedastic t test). Right
1058 panel: Cumulative distribution mIPSC frequency (p<0.0001; Kolmogorov-Smirnov
1059 test). **(e)** mIPSC amplitude in CA1 pyramidal neurons (Dlx-control sponge: range,
1060 from 21.5 to 34.6 pA; median, 25.9 pA; IQR, 4.0 pA. Dlx-miR-138 sponge: range,
1061 from 22.3 to 35.5 pA; median, 28.3 pA; IQR, 4.4 pA; n.s. p=0.13 Student's two-tailed

1062 heteroscedastic t test). Dlx-control sponge n=19 cells/2mice; Dlx-miR-138 sponge
1063 n=19cells/2mice.
1064 **Figure 4 – source data:** this file contains the raw data on which the graphs in Fig. 4
1065 are based.
1066
1067 **Figure 5**
1068 **(a)** Schematic overview of the strategy for generating miR-138 sponge^{PV} mice. **(b)**
1069 Beta-gal expression is largely restricted to PV expressing interneuron. Left panel:
1070 Representative picture from a CA1 region of a 138-sponge^{PV} hippocampal slice co-
1071 stained for the lacZ product beta-galactosidase (red) and PV (green). Scale bar=20
1072 μm. Right panel: quantification of PV+/lacZ+ cells in 138-sponge^{PV} mice. n=3 mice.
1073 **(c)** Behavioral characterization of 138-sponge^{PV} mouse line**,** upper: schematic
1074 representation of the Y maze novelty preference task; lower: exploration time spent
1075 in familiar (F) and novel (N) arm; 138-floxed n=10 mice; 138-sponge^{PV} n=10 mice;
1076 ***p=0.0002; n.s. p=0.19 (Mann-Whitney test). **(d)** Upper: schematic representation
1077 of the novel object recognition task; Lower: exploration time presented as
1078 percentage of total time spent with either novel or familiar object; 138-floxed n=10
1079 mice; miR-138 sponge n=10 mice; *p=0.035, n.s. p=0.57 (Student's two-tailed
1080 heteroscedastic t test). **(e)** Percentage of spontaneous alternations in the Y-Maze.
1081 138-floxed n=10; 138-sponge^{PV} n=10; n.s. p=0.90 (student's two-tailed
1082 heteroscedastic t-test)
1083 **Figure 5 – source data:** this file contains the raw data on which the graphs in Fig. 5
1084 are based.
1085
1086 **Figure 6:**
1087 **(a)** mIPSC frequency in CA1 pyramidal neurons. Upper panel: example traces, 138-
1088 floxed in orange, 138-songe^{PV} in red, scale bar: 50 pA, 200 ms. Lower panel: mIPSC
1089 frequency (138-floxed: range, from 1.6 to 10.2 Hz; median, 4.1 Hz; IQR, 1.5 Hz. 138-
1090 sponge^{PV}: range, from 3.6 to 15.2 Hz; median, 6.2 Hz; IQR, 4.2 Hz; ***p = 0.0002,
1091 Mann Whitney test). 138-floxed n=22 cells/5mice; 138-sponge^{PV} n=23cells/5mice. **(b)**
1092 PV+, VGAT+ bouton density. left panel: representative pictures (arrows point the
1093 PV+; VGAT+ boutons). middle panel: number of boutons per CA1 pyramidal neuron
1094 cell perimeter based on Hoechst counterstain. Right panel: VGAT puncta mean

1095 intensity; 138-floxed: n=73 cells/3 mice; 138-sponge^{PV}: n=95 cells/5 mice; data
1096 represents the average per mouse ± s.d; n.s., p=0.65 (bouton density), n.s.=0.59
1097 (mean intensity) (Student's two-tailed heteroscedastic t test); **(c)** Paired pulse ratio
1098 (PPR) of stimulated IPSCs in CA1 pyramidal neurons. Upper panel: example traces
1099 of PPR (inter stimulus interval of 100ms) for 138-floxed (orange) and 138-sponge^{ub}
1100 (red); scale bar: 100 pA, 50 ms. Lower panel: PPRs for different interstimulus
1101 intervals ranging from 50 ms to 150 ms (138-floxed vs. 138-sponge^{PV} [mean ± s.d.]:
1102 50 ms, 0.7 ± 0.2 vs. 0.7 ± 0.1 [n=13]; 100 ms: 0.8 ± 0.1 vs. 0.7 ± 0.1 [n=13]; 150 ms:
1103 0.7 ± 0.1 [n=12] vs. 0.7 ± 0.1. n.s. p=0.45, p=0.69, and p=0.89 for 50 ms, 100 ms
1104 and 150 ms, respectively. Mann Whitney test). **(d)** Unitary connections between
1105 presynaptic fast-spiking interneurons and postsynaptic CA1 pyramidal cells. Upper
1106 panel: example traces, 138-floxed: average of 50 sweeps in orange, 26 single
1107 sweeps in grey, 138-songe^{PV}: average of 50 sweeps in red, 26 single sweeps in
1108 grey; scale bar: 100 pA, 100 mV, 25 ms. Lower panel left: uIPSC amplitude (138-
1109 floxed: range, from 18.9 to 73.2 pA; median, 46.6 pA; IQR, 40.2 pA. 138-sponge^{PV}:
1110 range, from 19.3 to 123.8 pA; median, 64.5 pA; IQR, 64.4 pA; n.s. p=0.11 Student's
1111 two-tailed heteroscedastic t test). Lower panel right: Success rate (138-floxed: range,
1112 from 40 to 98 %; median, 86 %; IQR, 54 %. 138-sponge^{PV}: range, from 38 to 100 %;
1113 median, 98 %; IQR, 12 %; n.s. p=0.14 Mann Whitney Test). 138-floxed n=7
1114 pairs/3mice; 138-sponge^{PV} n=9 pairs/5mice. **(e)** Paired pulse ratio of unitary
1115 connections. Upper panel: example traces, 138-floxed in orange, 138-songe^{PV} in red,
1116 uIPSCs are normalized to the first uIPSC, scale bar: 100 mV, 50 ms. Lower panel:
1117 PPR ($2^{nd}/1^{st}$ uIPSC) (138-floxed: range, from 0.42 to 0.85; median, 0.56; IQR, 0.10.
1118 138-sponge^{PV}: range, from 0.44 to 0.62; median, 0.49; IQR, 0.14; n.s. p=0.34
1119 Student's two-tailed heteroscedastic t test). 138-floxed n=7 pairs/3mice; 138-
1120 sponge^{PV} n=9 pairs/5mice. **(f)** Coefficient of variation (138-floxed: range, from 0.38 to
1121 0.52; median, 0.44; IQR, 0.07. 138-sponge^{PV}: range, from 0.23 to 0.47; median,
1122 0.38; IQR, 0.15; *p= 0.028, Student's two-tailed heteroscedastic t test). 138-floxed
1123 n=7 pairs/3mice; 138-sponge^{PV} n=9 pairs/5mice.
1124 **Figure 6 – source data:** this file contains the raw data on which the graphs in Fig. 6
1125 are based.
1126
1127 **Supplementary Figure 1**

1128 **(a)** Relative luciferase activity in hippocampal neurons (DIV 12-17) transfected with
1129 pGL3 CTR (control) or pGL3-138 pbds (sensor) constructs. pGL3-CTR=1. n=3
1130 independent transfections. **p=0.0013 (One sample t test). **(b)** Relative luciferase
1131 activity in hippocampal neurons (DIV 12-17) transfected as in a), in addition with
1132 either control (100ng) or increasing amounts of 138 sponge (25-100ng). pGL3-
1133 CTR/pGL3-138 only = 1. n=3 independent transfections, **p=0.005, *p=0.032,
1134 #p=0.045 (student's two-tailed heteroscedastic t test). **(c)** Quantification of relative
1135 dendritic spine volume in rat hippocampal neurons (DIV10-18) transfected with GFP
1136 and increasing amounts (25-100ng) of either control or 138 sponge. GFP only = 1. n
1137 = 3 independent transfections; each value represents at least 150 spines per cell,
1138 from 6 individual neurons per experiment. **p=0.006, *p=0.027, #p=0.004 (student's
1139 two-tailed heteroscedastic t-test). **(d)** Representative enzymatic b-Gal staining of
1140 hippocampal slices obtained from 138-floxed mice (P21) injected with either saline
1141 (left) or rAAV-CMV-CRE (right). **(e)** Schematic of the sensor principle. **(f)** Activity
1142 counts of mice from indicated genotypes monitored over 24 h in their home cage;
1143 138-floxed: n=7 mice, 138-sponge$^{ub:}$ n=7 mice; data shown as mean ± s.d. **(g)**
1144 Percentage of spontaneous alternations in the Y-Maze. 138-floxed n=14 mice; 138-
1145 sponge^{ub} n=14 mice; p=0.43 (student's two-tailed heteroscedastic t-test). **(h, i)**
1146 Percentage of total distance travelled(h)/time spent(i) in the center of an open field
1147 arena during 30 min exploration by mice of the indicated genotypes; 138-floxed n=14
1148 mice; 138-sponge^{ub} n=14 mice; (h) p=0.30, (i) p=0.054 (Student's two-tailed
1149 heteroscedastic t test). **(j)** Percentage of total time spent in the open arms of an
1150 elevated plus maze (EPM) during 5 min exploration by mice of the indicated
1151 genotypes; 138-floxed: n=14 mice; 138-sponge^{ub}:n=14 mice; p=0.50 (Mann-Whitney
1152 test). **(k, l)** Cumulative distribution mEPSC amplitude (p=0.65; Kolmogorov-Smirnov
1153 test) (k) and frequency (p=0.85; Kolmogorov-Smirnov test) (l). **(m)** PPR of stimulated
1154 EPSCs in CA1 pyramidal neurons. Upper panel: example traces of PPR (inter
1155 stimulus interval of 50ms) for 138-floxed (orange) and 138-sponge^{ub} (blue); scale
1156 bar: 100 pA, 20 ms. Lower panel: PPRs for different interstimulus intervals ranging
1157 from 25 ms to 100 ms (138-floxed vs. 138-sponge^{ub} [mean ± s.d.]: 25 ms, 1.6 ± 0.1
1158 vs. 1.5 ± 0.2 [n=13]; 50 ms: 1.6 ± 0.2 vs. 1.5 ± 0.2 [n=13]; 75 ms: 1.4 ± 0.1 vs. 1.3 ±
1159 0.1 [n=11]; 100 ms: 1.3 ± 0.1 vs. 1.3 ± 0.1 [n=11]. n.s. p=0.14, 0.09, 0.17 and 0.13
1160 for 25, 50, 75 and 100 ms inter stimulus intervals, respectively. Mann-Whitney test.)

1161 **Suppl. Figure 1 – source data:** this file contains the raw data on which the graphs
1162 in suppl. Fig. 1 are based.
1163
1164 **Supplementary Figure 2**
1165 **(a)** Cumulative distribution plots of log_2-fold expression changes (138-sponge^{ub}/138-
1166 floxed) for genes either containing 7mer-1a (green), 7mer-m8 (red), 8mer (blue) or
1167 no (no site, black curve) predicted miR-138 binding sites. P-value is calculated
1168 compared to the no site population and indicated in the graph (KS-test). **(b)** Gene
1169 ontology (GO) term analysis for DEGs. Top ten enriched cellular component (CC)
1170 GO terms are shown. **(c)** Normalized expression levels, in single-cell clusters from
1171 Zeisel et al. (2018), of the genes upregulated in the miR-138 sponge. The genes
1172 are most abundantly expressed in inhibitory neurons. **(d)** Expression plots of
1173 selected miR-138 binding site containing transcripts in different neuronal subtypes
1174 (EXC: excitatory neurons; PV: parvalbumin+ interneurons; SST: somatostatin+
1175 interneurons; VIP: Vasoactive intestinal peptide+ interneurons based on
1176 http://research-pub.gene.com/NeuronSubtypeTranscriptomes/. **(e)** Expression of
1177 validated miR-138-5p targets based on RNA-seq in 138-floxed and 138-sponge^{Ub}
1178 mice. n=3 mice. Lypla1 n.s. p=0.90; Sirt1 n.s. p=0.66; Reln n.s. p=0.50 (student's
1179 two-tailed heteroscedastic t test).
1180 **Suppl. Figure 2 – source data:** this file contains the raw data on which the graphs
1181 in suppl. Fig. 2 are based.
1182
1183 **Supplementary Figure 3**
1184 **(a)** Quantification of miR-138-5p smFISH in Camk2a- and Erbb4-positive neurons.
1185 Camk2a-positive n=10 cells; ErbB4-positive n=7 cells, p=0.48 (student's two-tailed
1186 heteroscedastic t test). **(b)** Quantification of miR-138-5p levels in mouse brain tissue
1187 based on small RNA-seq data from (He et al., 2012) **(c)** Single-molecule FISH
1188 analysis of miR-138 (red) together with GFAP antibody stain (green) to label glia
1189 cells. Hoechst was used to counterstain nuclei. Arrow points to miR-138/MAP2
1190 positive, GFAP-negative neuron adjacent to glial cell. Scale bar=20 µm. **(d)** Single-
1191 molecule FISH analysis of Rims3 mRNA (green) together with Camk2a (grey; left) or
1192 Gad2 (grey; right) mRNA to label glutamatergic and GABAergic neurons,
1193 respectively. Scale bar=20 µm. **(e)** qPCR analysis of Rims3 mRNA in total
1194 hippocampal RNA obtained from 138-floxed or 138-sponge^{ub} mice. U6 snRNA was

1195 used for normalization. n=3 mice; *p=0.04 (Student's two-tailed heteroscedastic t
1196 test). **(f)** Relative luciferase activity in rat cortical neurons (DIV9-12) transfected with
1197 Rims3 3'UTR constructs with (138mut) or without (wt) a mutation in the miR-138
1198 binding site, together with miR-138 or negative control mimics. Negative control
1199 mimic = 1. n=3 independent transfections, *p=0.002, n.s. p= 0.23 (Student's two-
1200 tailed heteroscedastic t test). **(g)** Representative picture of primary rat hippocampal
1201 neurons infected with Dlx5/6-mCherry-138-sponge (red) and stained for GAD65/67
1202 (grey) and Hoechst (blue). Scale bar = 10 μm.
1203 **Suppl. Figure 3 – source data:** this file contains the raw data on which the graphs
1204 in suppl. Fig. 3 are based.
1205
1206 **Supplementary Figure 4**
1207 **a)** Cumulative distribution of mIPSC amplitude (p<0.0001; Kolmogorov-Smirnov
1208 test)**. b)** mIPSC rise (10-90%) and decay (90-10%) time. Left panel: mIPSC rise (10-
1209 90%) time (Dlx control sponge: range, from 1.0 to 2.1 ms; median, 1.5 ms; IQR, 0.4
1210 ms. Dlx miR-138 sponge: range, from 1.1 to 2.8 ms; median, 1.6 ms; IQR, 0.3 ms;
1211 n.s. p=0.76 Mann Whitney test). Right panel: mIPSC decay (90-10%) time (Dlx
1212 control sponge: range, from 9.6 to 13.4 ms; median, 10.0 ms; IQR, 0.6 ms. Dlx miR-
1213 138 sponge: range, from 9.7 to 10.8 ms; median, 10.1 ms; IQR, 0.4 ms; n.s. p=0.3
1214 Mann Whitney test). Dlx control sponge n=19 cells/2mice; Dlx miR-138 sponge
1215 n=19cells/2mice. **c)** Bar graphs of GFP/mCherry ratios from PV+ or PV- CA1
1216 hippocampal neurons in 138-floxed or 138-sponge^{Ub} mice infected with a 138-pbds
1217 sensor construct; 138-floxed/PV+: n=32(2 mice); 138-floxed/PV-: n=40(2 mice); 138-
1218 sponge/PV+: n=32(3 mice); 138-sponge/PV-: n=42(3 mice); n.s. p=0.113;* p=3.6x10^{-}
1219 ^{6} (Kolmogorov-Smirnov-Test). d) Venn diagram describing the overlap between
1220 transcripts upregulated in SCZ patients (Gandal et al., 2018) and miR-138 sponge
1221 mice (Fig. 2a). Fold enrichment = 1.43; p=0.00859 (Fisher test).
1222 **Suppl. Figure 4 – source data:** this file contains the raw data on which the graphs
1223 in suppl. Fig. 4 are based.
1224
1225 **Supplementary Figure 5**
1226 **(a-b)** Percentage of total distance travelled (a)/time spent (b) in the center of an
1227 open field arena during 30 min exploration by mice of the indicated genotypes; 138-

1228 floxed n=10 mice; 138-sponge^{PV} n=10 mice; (a) p=0.74 (b) p=0.28 (Student's two-
1229 tailed heteroscedastic t-test). **(c)** Percentage of total time spent in the open arms of
1230 an elevated plus maze (EPM) during 5 min exploration by mice of the indicated
1231 genotypes; 138-floxed n=10 mice; 138-sponge^{PV} n=10 mice; p=0.53 (Mann-Whitney
1232 test). **(d)** Time (s) mice spent freezing 24 h after the foot shock was administrated;
1233 138-floxed n=9 mice; 138-sponge^{PV} n=9 mice; p=0.075 (Student's two-tailed
1234 heteroscedastic t-test).
1235 **Suppl. Figure 5 – source data:** this file contains the raw data on which the graphs
1236 in suppl. Fig. 5 are based.
1237
1238 **Supplementary Figure 6**
1239 **(a-d)** mIPSC in CA1 pyramidal neurons. **(a)** Cumulative distribution of mIPSCs
1240 frequency. (p<0.0001; Kolmogorov-Smirnov test) **(b)** mIPSC amplitude (138-floxed:
1241 range, from 20.9 to 42.5 pA; median, 24.4 pA; IQR, 5.0 pA. 138-sponge^{PV}: range,
1242 from 18.0 to 41.6 pA; median, 25.7 pA; IQR, 4.0 pA; n.s. p=0.22 Mann Whitney test).
1243 **(c)** cumulative distribution of mIPSCs amplitude (p<0.0001 Kolmogorov-Smirnov
1244 test). 138-floxed n=22 cells/5mice; 138-sponge^{ub} n=23cells/5mice. **(d)** mIPSC rise
1245 (10-90%) and decay (90-10%) time. Left panel: mIPSC rise (10-90%) time (138-
1246 floxed: range, from 1.4 to 2.7 ms; median, 1.9 ms; IQR, 0.4 ms. 138-sponge^{PV}:
1247 range, from 1.3 to 2.5 ms; median, 2.0 ms; IQR, 0.4 ms; n.s. p=0.28 Mann Whitney
1248 test). Right panel: mIPSC decay (90-10%) time (138-floxed: range, from 9.9 to 13.6
1249 ms; median, 11.1 ms; IQR, 0.9 ms. 138-sponge^{PV}: range, from 9.5 to 14.2 ms;
1250 median, 11.6 ms; IQR, 1.8 ms; n.s. p=0.20 Mann Whitney test). 138-floxed n=22
1251 cells/5mice; 138-sponge^{ub} n=23cells/5mice. **(e)** Density of PV+ interneurons in CA1
1252 hippocampus of mice with the indicated genotype. Values are expressed relative to a
1253 defined region of interest (ROI). 138-floxed: n=16 ROIs/4 mice; 138-sponge^{PV}: n=18
1254 ROIs/5 mice; data represents the average per mouse ± s.d.; n.s. p=0.8049 (Mann-
1255 Whitney test). **(f)** Properties of fast-spiking interneurons. Upper panel: example
1256 traces, 138-floxed in orange, 138-songe^{PV} in red, scale bar: 50 mV, 500 ms. Lower
1257 panel left: spiking frequency (138-floxed: range, from 123 to 159 Hz; median, 143
1258 Hz; IQR, 29 Hz. 138-sponge^{PV}: range, from 96 to 170 Hz; median, 118 Hz; IQR, 46
1259 Hz; n.s. p=0.31 Student's two-tailed heteroscedastic t test). Lower panel middle:
1260 input resistance (138-floxed: range, from 40 to 60 MΩ; median, 57 MΩ; IQR, 18 MΩ.
1261 138-sponge^{PV}: range, from 30 to 71 MΩ; median, 33 MΩ; IQR, 26 MΩ; n.s. p=0.22

1262 Mann Whitney test). Lower panel right: resting membrane potential (138-floxed:
1263 range, from -68 mV to -62 mV; median, -64 mV; IQR, 4.5 mV. 138-sponge^{PV}: range,
1264 from -70 to -56 mV; median, -67 mV; IQR, 9 mV; n.s. p=0.78 Student's two-tailed
1265 heteroscedastic t test). 138-floxed n=5 cells/3mice; 138-sponge^{ub} n=5cells/5mice
1266 **Suppl. Figure 6 – source data:** this file contains the raw data on which the graphs
1267 in suppl. Fig. 6 are based.

Figure 1

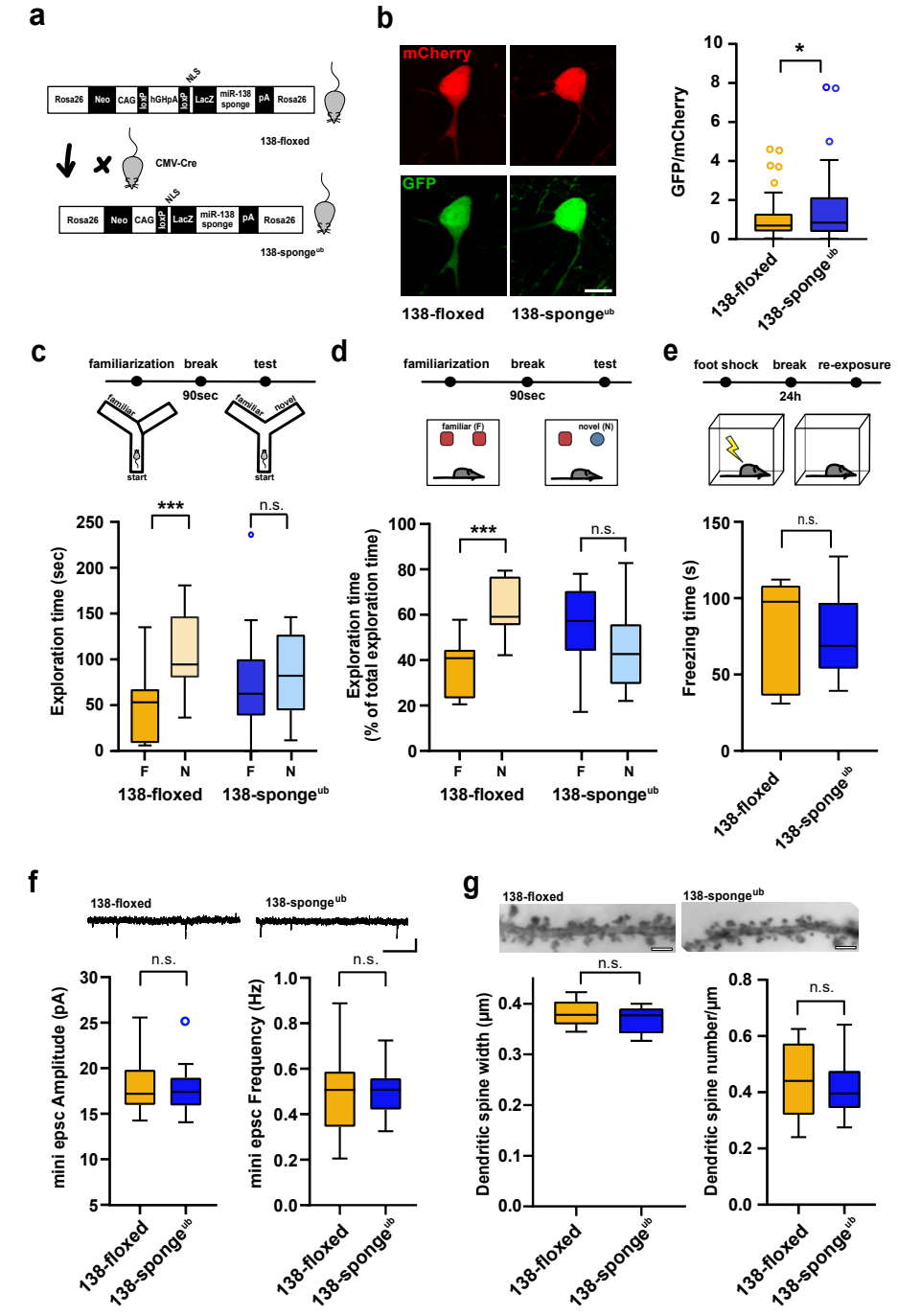
a
Rosa26
Neo
CAG
hGHpA
NLS
LacZ
miR-138 sponge
pA
Rosa26
138-floxed
CMV-Cre
138-sponge^ub
b
mCherry
GFP
138-floxed
138-sponge^ub
GFP/mCherry
*
c
familiarization
break
test
90sec
familiar
novel
start
Exploration time (sec)
***
n.s.
F
N
138-floxed
138-sponge^ub
d
familiarization
break
test
90sec
familiar (F)
novel (N)
Exploration time (% of total exploration time)
***
n.s.
e
foot shock
break
re-exposure
24h
Freezing time (s)
n.s.
f
138-floxed
138-sponge^ub
mini epsc Amplitude (pA)
mini epsc Frequency (Hz)
n.s.
g
Dendritic spine width (µm)
Dendritic spine number/µm
n.s.

Figure 2

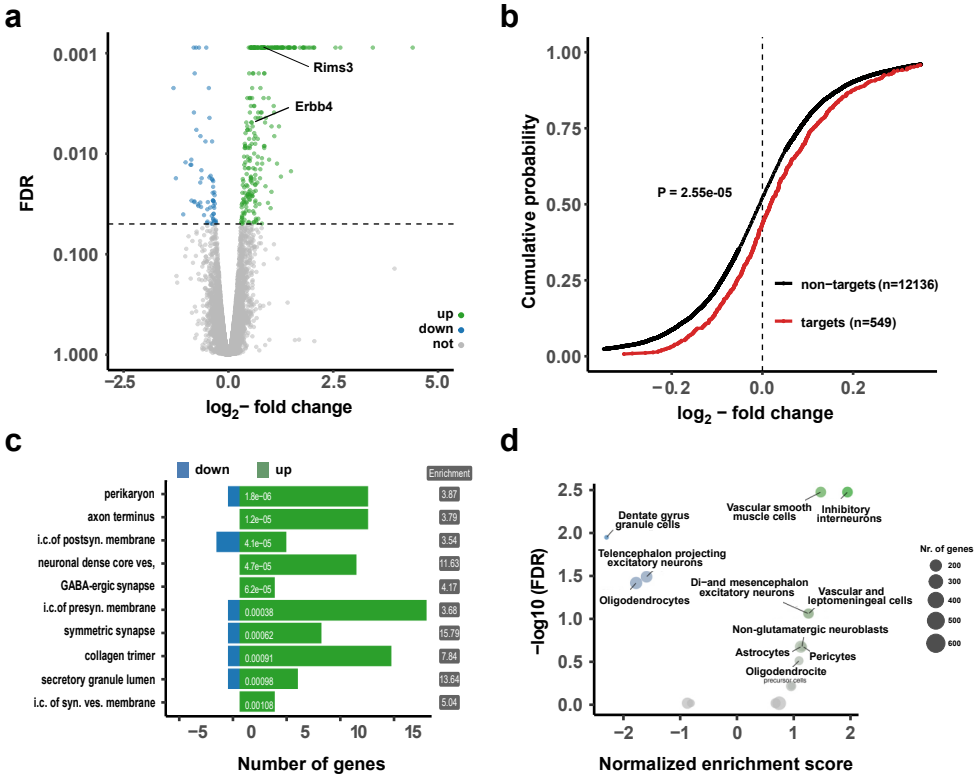
a
Rims3
Erbb4
FDR
0.001
0.010
0.100
1.000
up
down
not
−2.5
0.0
2.5
5.0
log2− fold change
b
Cumulative probability
1.00
0.75
0.50
0.25
0.00
P = 2.55e-05
non−targets (n=12136)
targets (n=549)
−0.2
0.0
0.2
log2 − fold change
c
down
up
Enrichment
perikaryon
axon terminus
i.c.of postsyn. membrane
neuronal dense core ves,
GABA-ergic synapse
i.c.of presyn. membrane
symmetric synapse
collagen trimer
secretory granule lumen
i.c. of syn. ves. membrane
1.8e−06
1.2e−05
4.1e−05
4.7e−05
6.2e−05
0.00038
0.00062
0.00091
0.00098
0.00108
3.87
3.79
3.54
11.63
4.17
3.68
15.79
7.84
13.64
5.04
−5
0
5
10
15
Number of genes
d
−log10 (FDR)
2.5
2.0
1.5
1.0
0.5
0.0
Dentate gyrus granule cells
Vascular smooth muscle cells
Inhibitory interneurons
Telencephalon projecting excitatory neurons
Oligodendrocytes
Di−and mesencephalon excitatory neurons
Vascular and leptomeningeal cells
Non-glutamatergic neuroblasts
Astrocytes
Pericytes
Oligodendrocite precursor cells
Nr. of genes
200
300
400
500
600
−2
−1
0
1
2
Normalized enrichment score

Figure 3

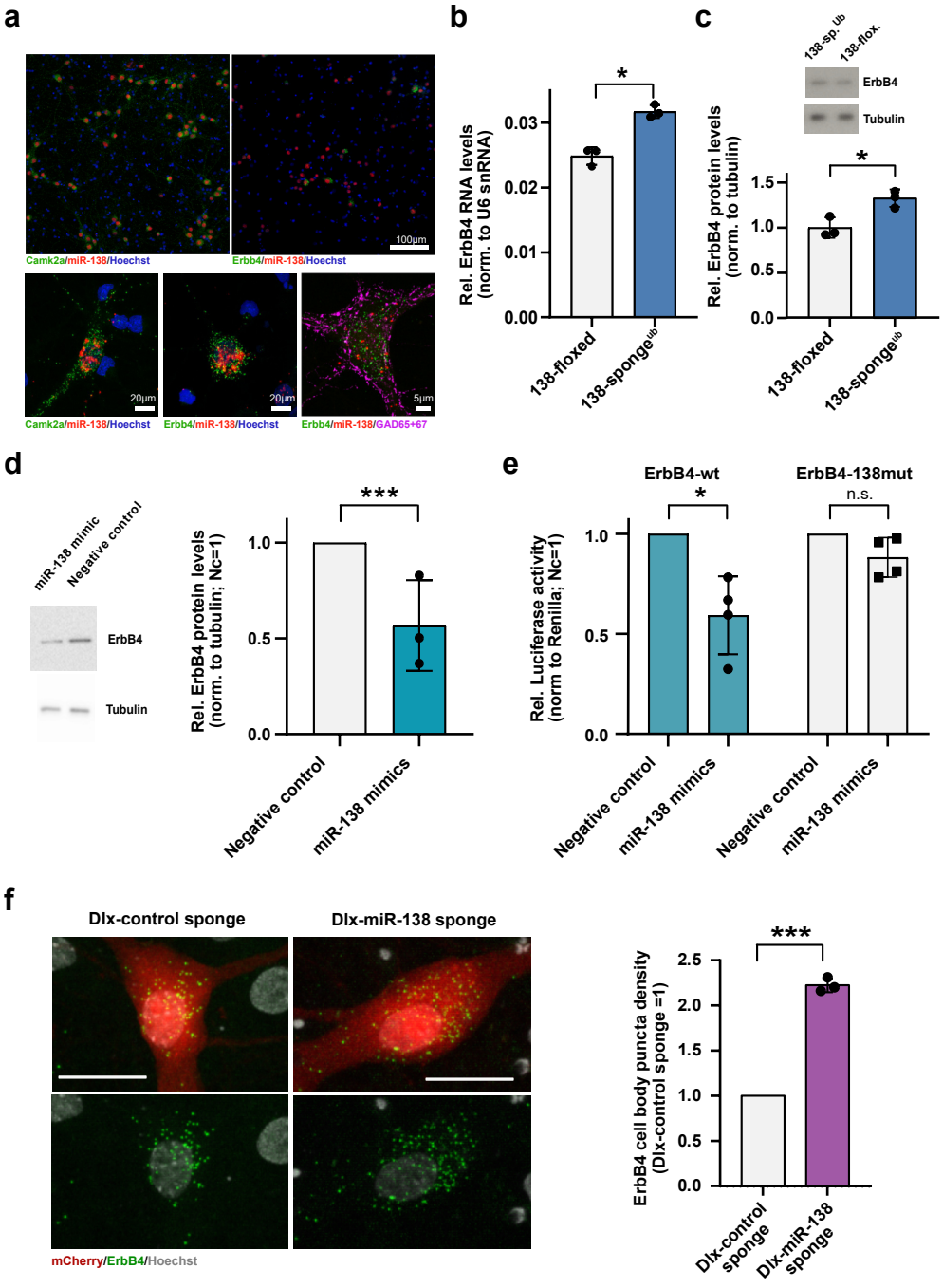
a
Camk2a/miR-138/Hoechst
Erbb4/miR-138/Hoechst
100µm
20µm
20µm
5µm
Camk2a/miR-138/Hoechst
Erbb4/miR-138/Hoechst
Erbb4/miR-138/GAD65+67
b
Rel. ErbB4 RNA levels (norm. to U6 snRNA)
0.03
0.02
0.01
0.00
*
138-floxed
138-sponge^Ub
c
138-sp. Ub
138-flox.
ErbB4
Tubulin
Rel. ErbB4 protein levels (norm. to tubulin)
1.5
1.0
0.5
0.0
*
138-floxed
138-sponge^Ub
d
miR-138 mimic
Negative control
ErbB4
Tubulin
Rel. ErbB4 protein levels (norm. to tubulin; Nc=1)
1.0
0.5
0.0
***
Negative control
miR-138 mimics
e
ErbB4-wt
ErbB4-138mut
*
n.s.
Rel. Luciferase activity (norm to Renilla; Nc=1)
1.0
0.5
0.0
Negative control
miR-138 mimics
Negative control
miR-138 mimics
f
Dlx-control sponge
Dlx-miR-138 sponge
mCherry/ErbB4/Hoechst
ErbB4 cell body puncta density (Dlx-control sponge =1)
2.5
2.0
1.5
1.0
0.5
0.0
***
Dlx-control sponge
Dlx-miR-138 sponge

Figure 4

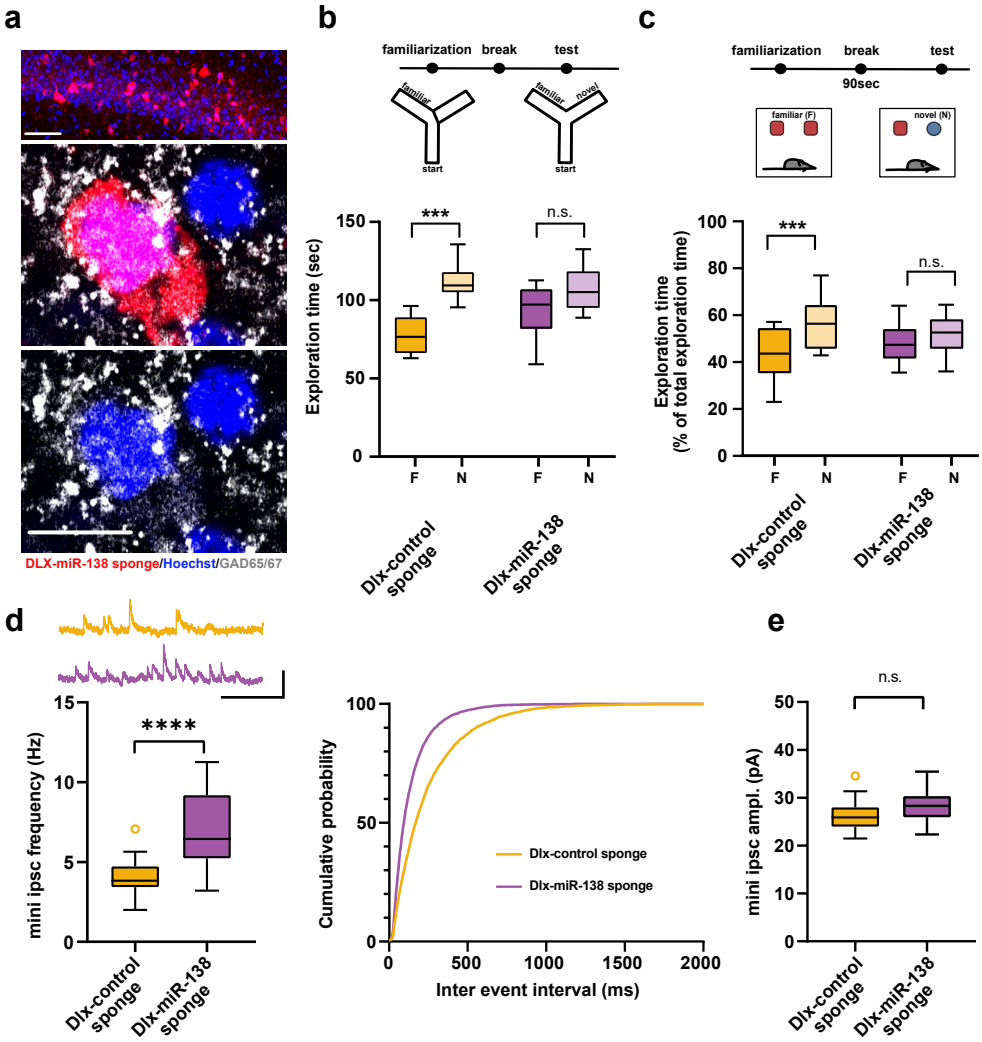
a
DLX-miR-138 sponge/Hoechst/GAD65/67
b
familiarization
break
test
familiar
novel
start
Exploration time (sec)
***
n.s.
F
N
Dlx-control sponge
Dlx-miR-138 sponge
c
90sec
familiar (F)
novel (N)
Exploration time (% of total exploration time)
d
mini ipsc frequency (Hz)
****
Cumulative probability
Inter event interval (ms)
e
mini ipsc ampl. (pA)

Figure 5

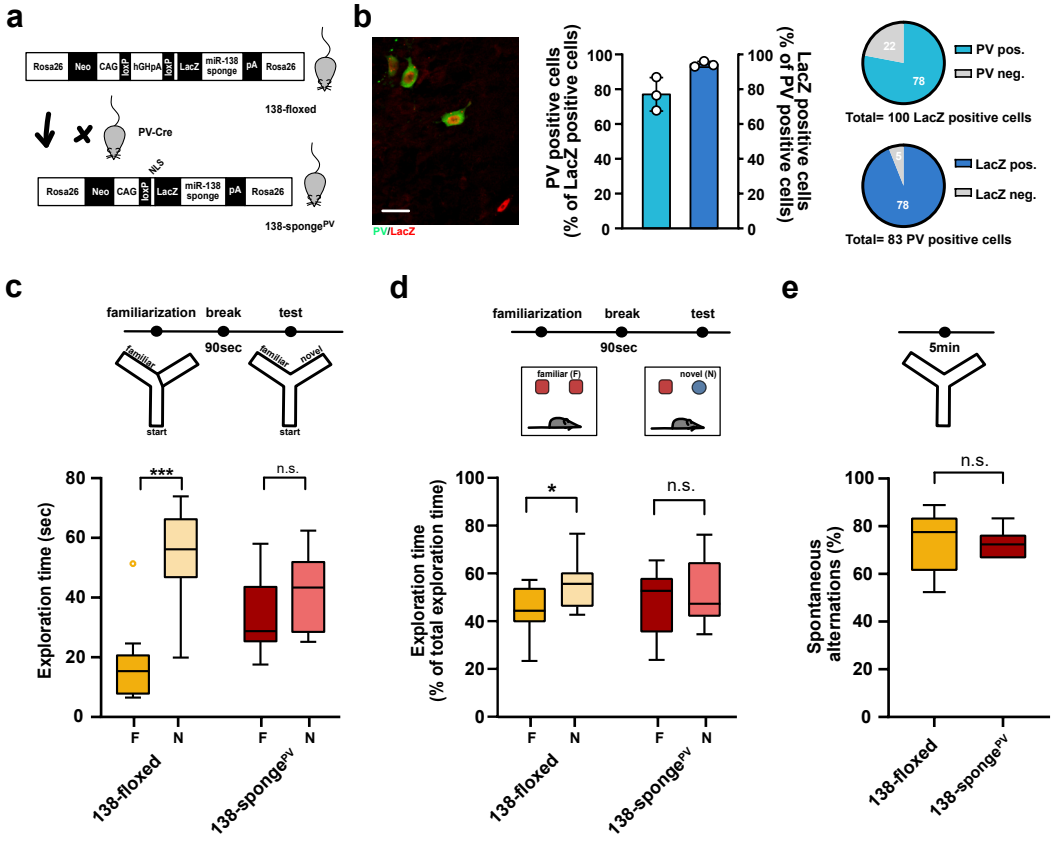
a
Rosa26
Neo
CAG
loxP
hGHpA
loxP
LacZ
miR-138 sponge
pA
Rosa26
138-floxed
PV-Cre
NLS
138-sponge^PV
b
PV/LacZ
PV positive cells (% of LacZ positive cells)
LacZ positive cells (% of PV positive cells)
PV pos.
PV neg.
Total= 100 LacZ positive cells
LacZ pos.
LacZ neg.
Total= 83 PV positive cells
c
familiarization
break
test
90sec
familiar
novel
start
Exploration time (sec)
***
n.s.
F
N
138-floxed
138-sponge^PV
d
familiar (F)
novel (N)
Exploration time (% of total exploration time)
*
e
5min
Spontaneous alternations (%)

Figure 6

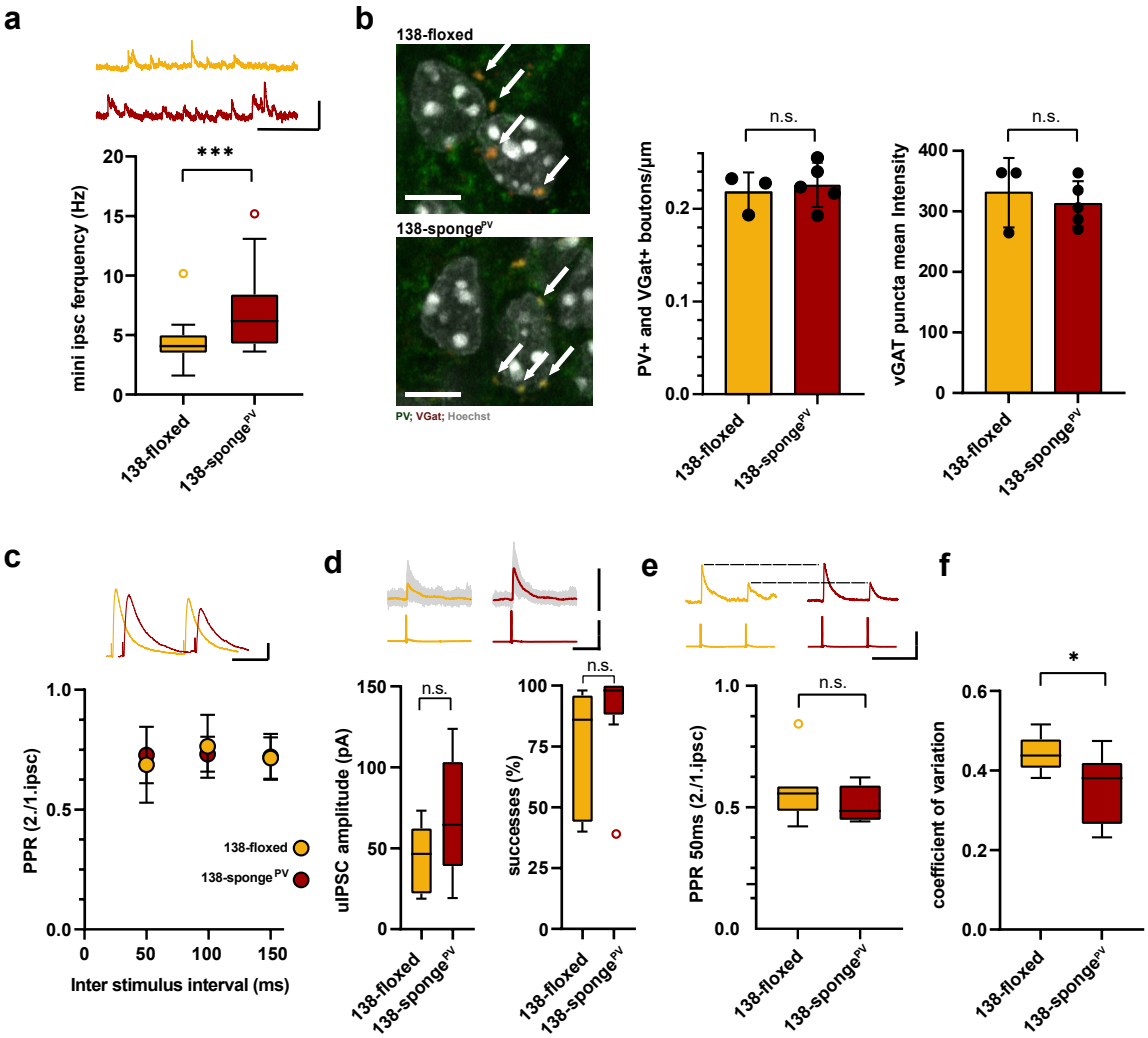
a
mini ipsc ferquency (Hz)
***
138-floxed
138-sponge PV
b
138-floxed
138-sponge PV
PV; VGat; Hoechst
PV+ and VGat+ boutons/µm
n.s.
vGAT puncta mean Intensity
n.s.
c
PPR (2./1.ipsc)
138-floxed
138-sponge PV
Inter stimulus interval (ms)
d
uIPSC amplitude (pA)
n.s.
successes (%)
n.s.
e
PPR 50ms (2./1.ipsc)
n.s.
f
coefficient of variation
*

Supplementary Figure1

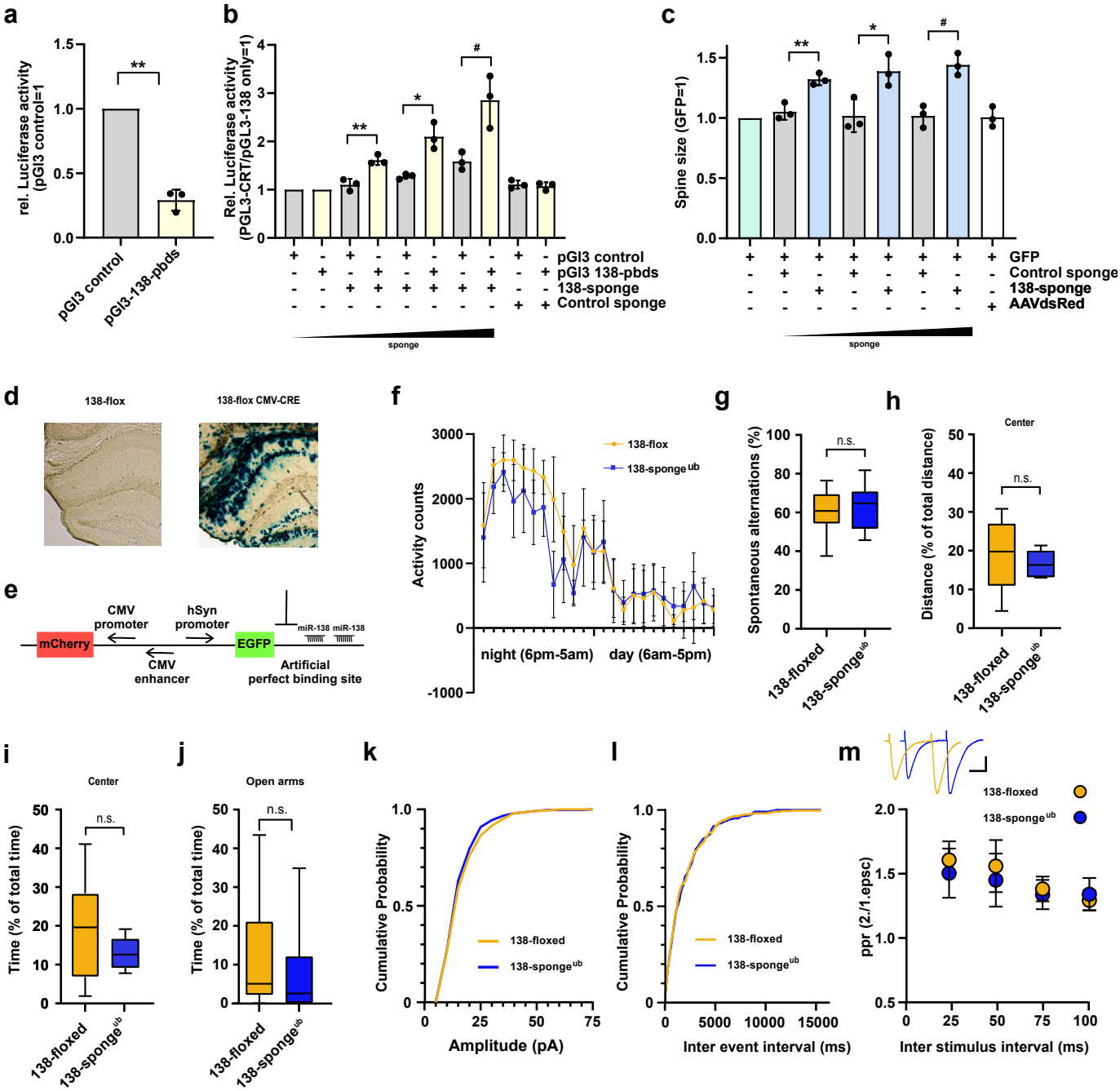

Supplementary Figure 2

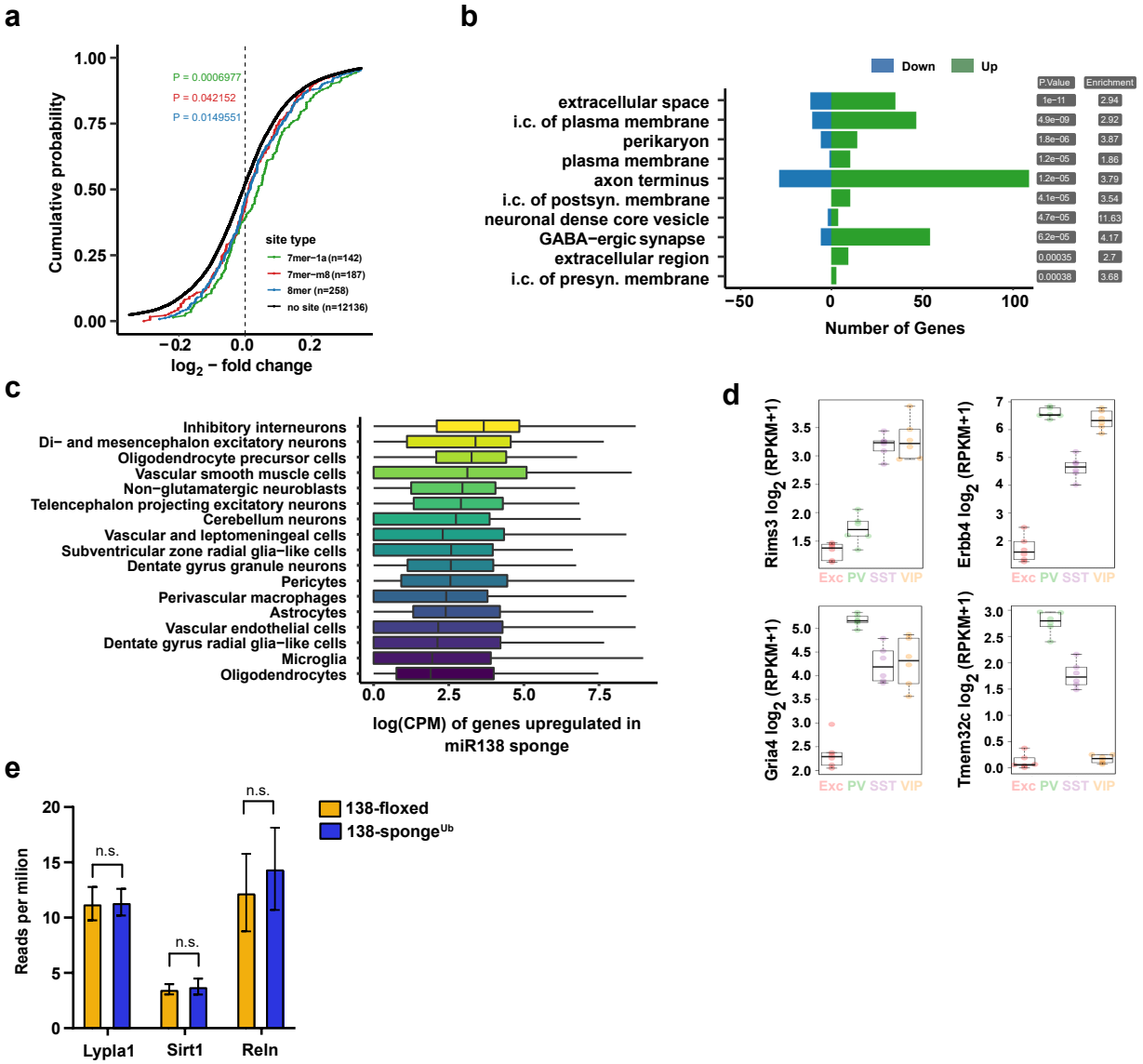

Supplementary Figure 3

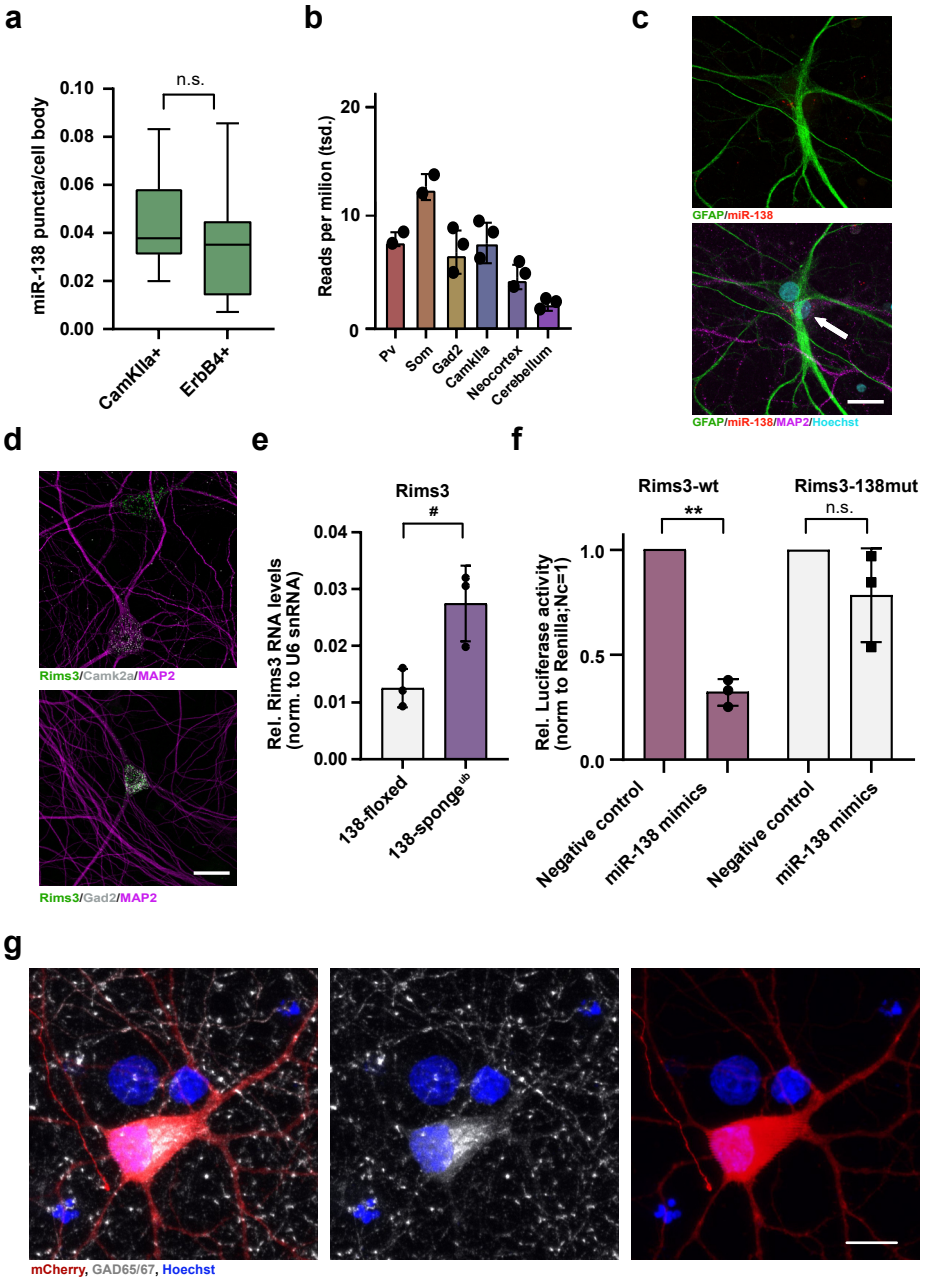

Supplementary Figure 4

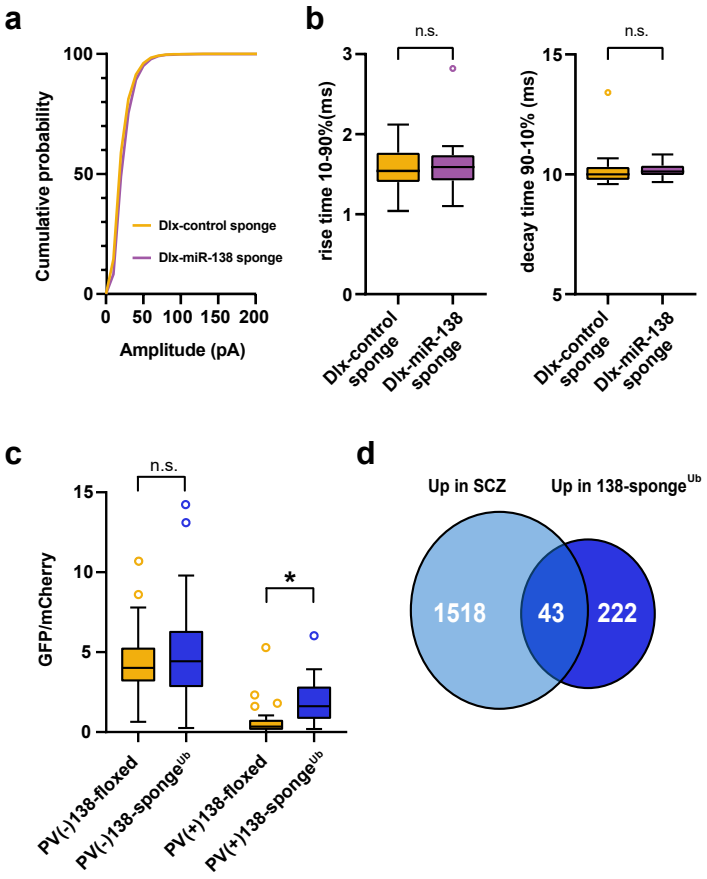

Supplementary Figure 5

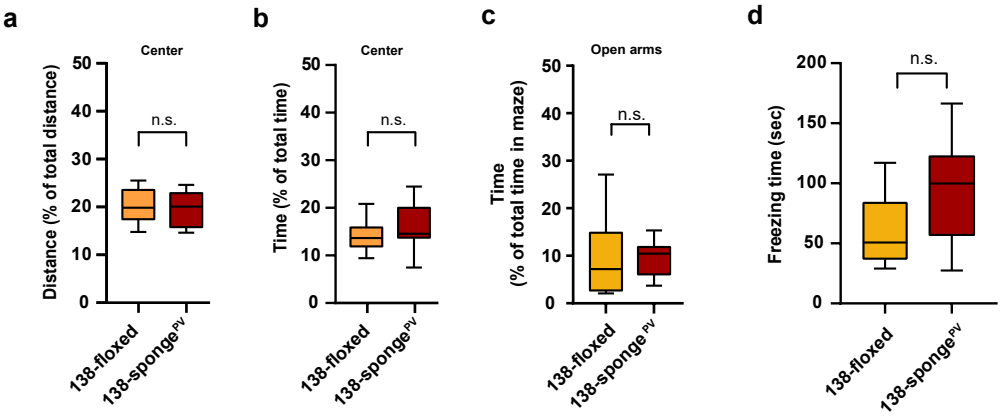
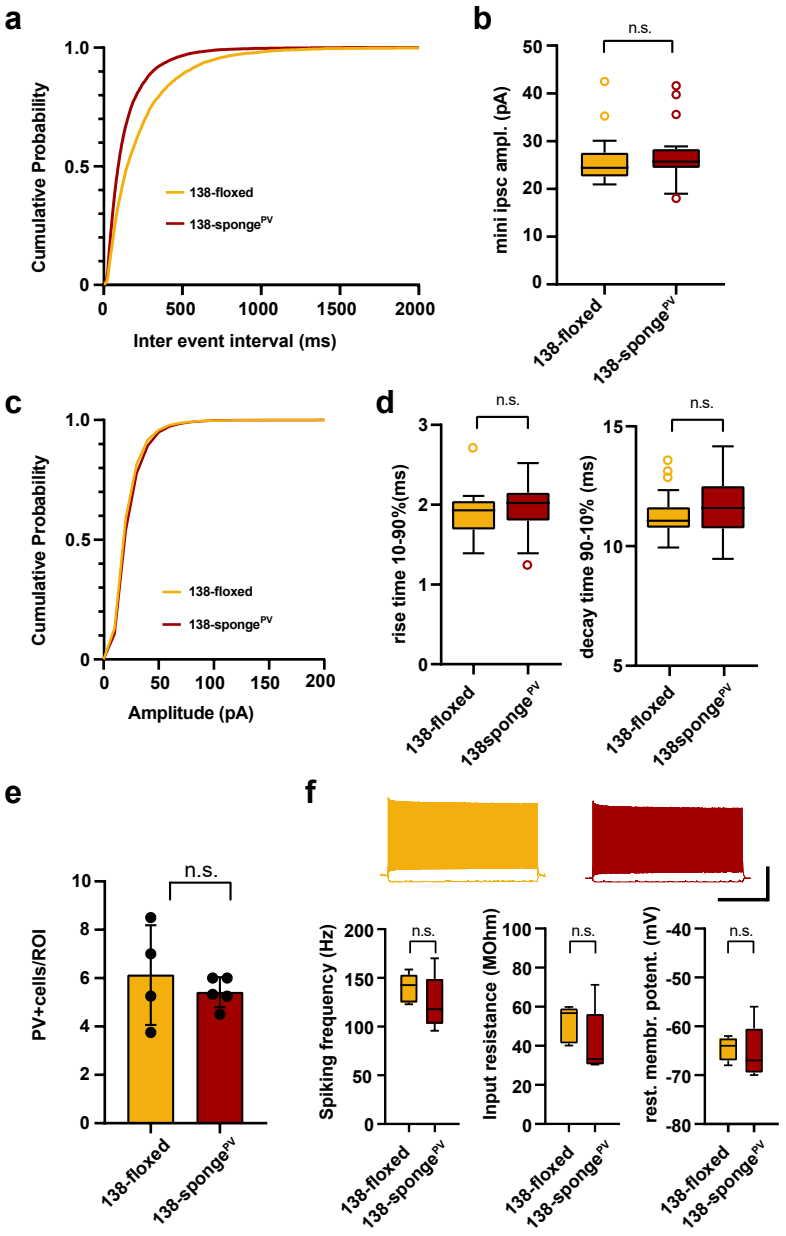
Supplementary Figure 6